

POLITECNICO DI TORINO

Master Degree in
Communication and Computer Networks Engineering

Master's Thesis

**Optimization of modern
ultra-high bitrate optical fiber
links**



Supervisor

Prof. Roberto Gaudino

External Supervisor:

Dr. Pierluigi Debernardi

Candidate

Giuseppe Caruso

ACADEMIC YEAR 2018-2019

Summary

The development and spread of cloud services is requiring data and resources to be easily and quickly available. As most of these traffic is generated and/or processed in data centers, the natural consequence is that they need to reach higher and higher performances in order to keep up, being at the same time economically and energetically viable. The introduction of Vertical Cavity Surface Emitting Laser (VCSEL) in optical transmitters turned out to be precious, proving to be a key technology enabler for high-speed short-range interconnects (i.e. for intra-datacenter links below 200 meters). This particularly holds true for datacenters, due to VCSEL low production costs, low power consumption and good modulation capabilities compared to edge-emitting lasers (EEL). In this scenario, numerical models become invaluable tools in order to simulate the behavior of transmission systems, as they can provide indications of the performance-limiting factors and, possibly, suggests optimizations and improvements.

This work aimed to create a numerical time-domain simulator of a VCSEL-based optical TX-RX link, with most emphasis being put on the modelling of a VCSEL as an optical transmitter.

Since coherent light emission in lasers is the result of the interaction between optical and electrical phenomena, a complete and accurate modelling of these devices is not an easy task. Moreover, thermal effects have a relevant impact on VCSEL performance, in terms of output power and modulation bandwidth. However in this thesis, by making some approximations, it has been possible to obtain a simple lumped model based on rate equations, that resulted efficient in its implementation and at the same time accurate enough when compared to a real device.

First, static characteristics were studied and implemented: an analytical formula to relate light output versus current input (PI curve) was derived for the steady state and compared to the numerical solution of the rate equation, obtained using Runge Kutta 4th order method. After that, simulation parameters were optimized in order to get an output curve comparable to VCSEL measurements provided by OptiGOT (a startup based in Göteborg, Sweden, that designs and produces VCSELs), so that the subsequent simulations could be compared to those of real devices.

A dynamic characterization model was then implemented: the rate equations were

linearized around a bias point and a small-signal analytical transfer function was derived, which provided a validation of the numerical code (shown in Figure 1a). The simulations were then compared to experimental results, again on OptiGOT VCSELs. Misalignment between the simulated and the measured curves was attributed to bandwidth-limiting effects of parasitics. After deriving an equivalent circuit model for the VCSEL parasitics, their effects were modeled as a low-pass first order filter. The addition of parasitics to the small signal response provides a better fit to the measured curves, anyway leftover inconsistencies suggests the need of a more complex equivalent circuit.

Third step was the implementation of the Relative Intensity Noise (RIN) model: even in absence of modulation, real devices show fluctuations in the output power due to spontaneous generation and recombination of carriers and photons. These variations are quantified by the RIN. In our numerical model, RIN is implemented by adding two Langevin noise terms (one for the carriers and one for the photons) in the rate equations. The resulting output was compared to the available analytical formula and coherence between expected and simulated results was proven (Figure 1b).

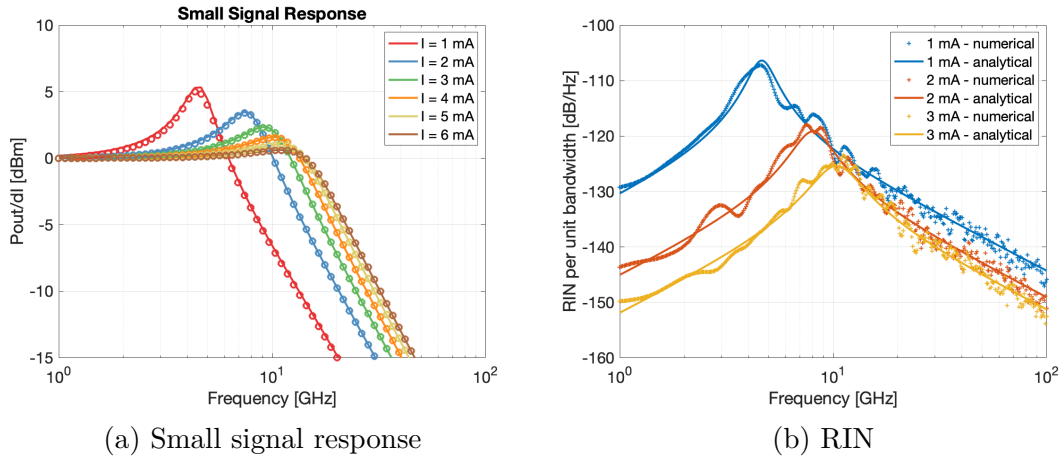


Figure 1: Dynamic characteristics at different bias points - Full line is the analytical curve, dots report the numerical results

After having verified the consistency of the model, a simplified communication link was simulated, to evaluate the performance of the device under large-signal modulation. First, a binary PAM-2 (NRZ) modulation was considered. Simulations were done using random sequences and choosing suitable current levels, the modulated input current was generated, filtered and input to the VCSEL. The numerical solution of the rate equations provides the evolution in time of VCSEL instantaneous output power, as shown in Figure 2. Initial attempts on PAM-4 modulation were also undertaken.

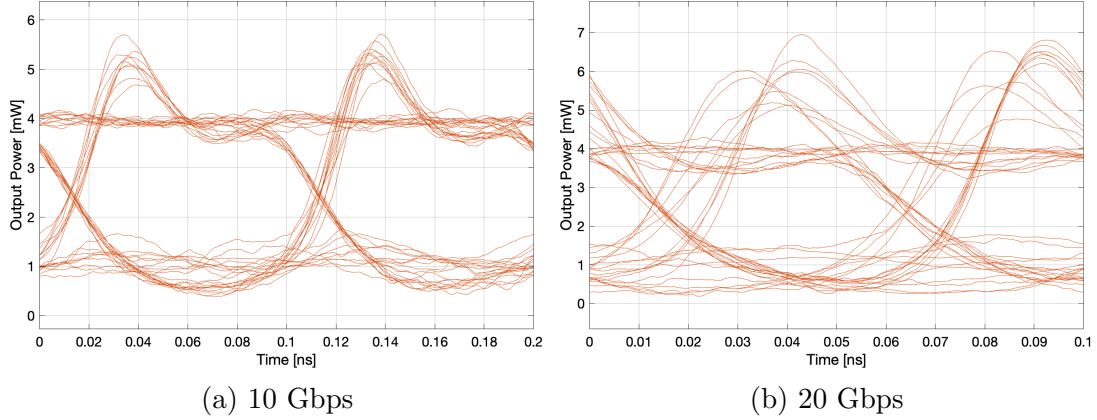


Figure 2: Eye diagram of VCSEL output power (PAM-2 NRZ modulation)

Last, laboratory tests on VCSELs were performed: DC characteristics, electrical S-parameters and spectrum were measured and then are reported, together with the setups used in the various tests. Even though no on-wafer measurements were performed, a quick overview of the process is described for future reference.

Considering the work done, improvements can still be made: as regards the VCSEL model, the inclusion of thermal effects can better approximate device behavior at higher currents, while a more accurate description of parasitics could provide accuracy improvements in terms of bandwidth capabilities. Regarding the transmission link implementation, Bit Error Rate (BER) evaluation should be the next step, after accounting for receiver noise and fiber effects on the transmitted signal. Nonetheless, accounting for the approximations described at the beginning, the implemented model provided consistent results both with analytical formulas and measured data, together with good simulation times. If paired with measurements on real devices, it can be optimized to provide a good base model to simulate VCSEL behavior under large signal modulations and develop more articulated TX/RX schemes.

Acknowledgements

Contents

List of Tables	8
List of Figures	9
1 Introduction	12
1.1 A short introduction to VCSEL	14
1.2 VCSEL: main building blocks	14
1.2.1 VCSEL vs EEL	16
1.3 VCSEL in telecommunications	16
1.3.1 State of the art	18
1.4 Motivations for this thesis	20
1.4.1 Thesis outline - WORK IN PROGRESS	20
2 VCSEL modelling	21
2.1 Static characteristics	24
2.2 Dynamic analysis	26
2.3 Small Signal Frequency Response	29
2.4 Some hints on parasitics	31
2.5 Noise Analysis	33
2.6 Conclusions	36
3 Large signal modulation	39
3.1 PAM-2 (NRZ) modulation	41
3.2 PAM-4 modulation	44
3.3 Conclusions	46
4 Experimental measurements	47
4.1 DC characteristics - PI curve	48
4.1.1 Setup	48
4.1.2 Results	50
4.2 Electrical S-parameters	52
4.2.1 Setup	52

4.2.2	Results	52
4.3	Spectrum measurements	52
4.3.1	Setup	52
4.3.2	Results	53
4.4	Conclusions	53
4.5	Appendix: hints for on-wafer measurements	54
5	Conclusions	59
	Bibliography	61

List of Tables

1.1	Edge Emitting Laser vs VCSEL	18
2.1	List of parameters used in the simulations	25
3.1	PAM-4 bias currents	44
4.1	Laboratory equipment used	50

List of Figures

1.1	Datacenter traffic growth	13
1.2	2019 Ethernet Roadmap	13
1.3	Generation and recombination mechanisms	15
1.4	Schematic cross-section of a VCSEL	17
1.5	Section of EEL and VCSEL	17
1.6	VCSEL configurations	19
1.7	SWDM4 Transceiver Block Diagram	19
2.1	Gain fit	23
2.2	VCSEL PI curve	25
2.3	Carrier and photon density over time	26
2.4	aaa	27
2.5	Small signal modulation response for a real device at different currents	30
2.6	Simulated Small Signal Response	31
2.7	Small signal model including driving source	32
2.8	Filtered small signal response vs. measured curve	34
2.9	Small Signal Response - comparison after adding parasitics	35
2.10	RIN	37
2.11	Analytical RIN vs. rate equations	38
3.1	Block diagram of the implemented modulation scheme	39
3.2	Block diagram of the implemented modulation scheme	40
3.3	Binary modulation scheme - block diagram	41
3.4	PAM-2 - Modulation current and resulting output power	41
3.5	PAM-2 - Effects of RIN at 10 Gbps	42
3.6	PAM-2 - Effects of RIN at 20 Gbps	43
3.7	PAM-2 modulation - attempts at 30 Gbps	43
3.8	PAM-4 - block diagram	44
3.9	PAM-4 - Modulation current and resulting output power	44
3.10	VCSEL output power - PAM-4 modulation	45
4.1	OptiGOT VCSEL	47
4.2	ULM VCSEL - provided characteristics	48
4.3	VCSEL packages	49
4.4	Fiber alignment stage	49

4.5	Block diagram of the DC characteristics measurement setup	50
4.6	Measured DC characteristics	50
4.7	Block diagram of setup for coupling loss measurements	51
4.8	Coupling loss	51
4.9	Block diagram of the S-parameters measurement setup	52
4.10	Measured S_{11} response	53
4.11	Measured S_{21} response	54
4.12	Block diagram of the spectrum measurement setup	54
4.13	Newfocus 1484-A-50 measured frequency response	55
4.14	VCSEL spectra at various currents	56
4.15	On-wafer measurement testbed	57
4.16	Typical dimensions of on-wafer bond pad	58
4.17	Probes for on-wafer testing	58

Chapter 1

Introduction

Today it is very hard to imagine everyday life without Internet, as more and more activities take place online. Behind the apparent user-friendliness of most applications lies a huge interconnection network that must be capable of handling the transfer of ever increasing amounts of data. While fixed networks were historically based on copper, fiber optical communications quickly became a fundamental asset, mainly for two reasons: much higher capacity and much smaller losses and attenuation with respect to copper cables. To have an idea of the huge potential of fiber optics for telecommunications, it is enough to think that the first transatlantic optical cable was put in place in 1988, TAT-8, carried 280 Mbit/s. 30 years later, in February 2018, *MAREA*, a transatlantic cable funded by Microsoft and Facebook, began its operations, allowing transmission speeds of up to 160 Tbit/s (8 fiber pairs at 20 Tbit/s) and in 2019 a team of researchers achieved speeds of 26.2 Tbit/s on the same cable [1]. At the same time, ongoing development and spread of cloud services is requiring data and resources to be easily and quickly reachable, leading to the expansion of datacenters, both in number, dimensions and, most important, network capacity; Cisco estimates that 20.7 ZB of traffic will cross data centers in 2021 (Figure 1.1).



Figure 1.1: Datacenter traffic growth [2]

Clearly, this increase in traffic capacity goes hand in hand with higher and higher bitrate requirements: by taking a look at the Ethernet standard roadmap in Figure 1.2, current trends aim to 100 and 400 Gbit/s, but 800 Gbit/s and 1.6 Tbit/s are already planned, with release expected in the 2020-2030 decade [3].

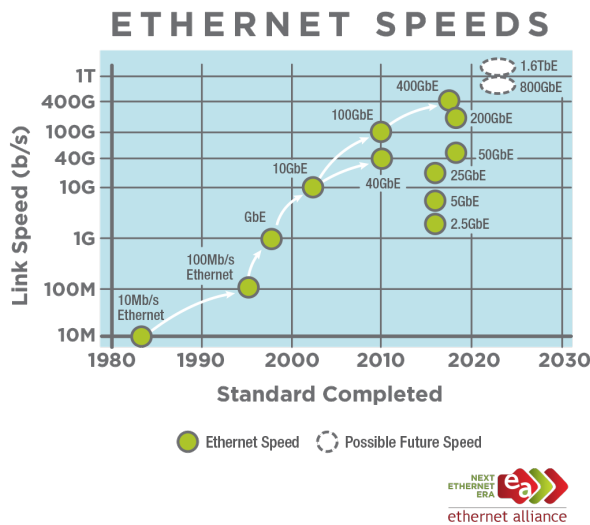


Figure 1.2: 2019 Ethernet Roadmap [4]

It goes without saying that copper transmission capabilities can hardly keep up, making fiber optics interconnects the main reasonable choice for short-reach links. In this scenario there is therefore a need also for transceivers with minimum footprint, low-cost, energy efficient and capable of managing higher and higher bitrates.

The work of this thesis aims to create a software simulator that emulates a high-bitrate short-range communication system, in order to analyze its performance and optimize its parameters. Most emphasis is placed on the implementation of a VCSEL-based transmitter, whose creation, development and implementation as an optical transmitter made it one of the key technology enabler for high-bitrate short range communications.

1.1 A short introduction to VCSEL

Vertical Cavity Surface Emitting Lasers (VCSEL) are a family of diode lasers that, as the name suggests, emit light vertically (orthogonal to the wafer surface). VCSEL is a relatively recent invention, as it was created in 1979 by Prof. Kenichi Iga [5], but since then research and development on these devices has achieved huge leaps forward. Room temperature operation was obtained in 1984 [6], while in 1988 the first continuous wave (CW) device working at room temperature was demonstrated, emitting at 850 nm. In the middle of the 1990s Honeywell became selling the first commercial products [7]. Today, VCSEL proved to be a versatile technology in a variety of sectors and applications, such as:

- Computer mice sensors
- Proximity sensors
- Automotive applications, for example LIDAR [8]
- Atomic clocks [9, 10, 11]
- Laser printers [12]
- Medical applications [13, 14]
- High-power applications [15]
- Data centers

It is estimated that 1 billion VCSELs have been shipped up to 2013, furthermore the introduction of facial recognition capabilities in smartphones has led to a huge increase in production [16]. Global revenues for the VCSEL market are expected to reach \$ 1 billion in 2022.

1.2 VCSEL: main building blocks

The description of the main working mechanisms of a diode laser is of great help in order to understand how VCSELs work. Diode lasers are basically made of a gain

material embedded into a resonant cavity. To understand how the gain material works, it is useful to have a basic idea on the energy levels associated to the electrons in the gain medium. Considering a simplified model, we can say that electrons can occupy either a valence or a conduction band, with the conduction band having the higher energy. Three main types of transitions between the two bands exist:

- a photon with energy $E \approx E_2 - E_1$ can be absorbed by the system and stimulate an electron to move from the lower to the higher energy band, creating a hole in the valence band
- an electron in the conduction band can spontaneously recombine with a hole in the valence band, causing the emission of a photon with random direction and phase; this is called Spontaneous Emission
- an incident photon can cause the recombination of an electron-hole pair with the consequent generation of another photon, with the same direction and phase of the incident one; this is the main mechanism of light generation in lasers and is called Stimulated Emission.

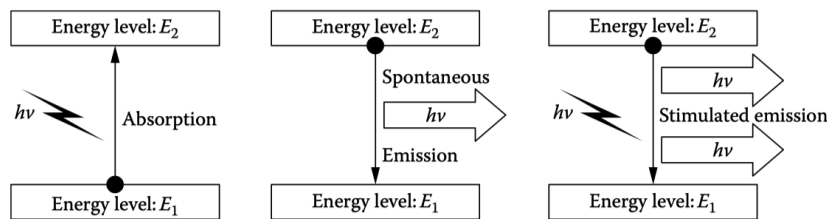


Figure 1.3: Generation and recombination mechanisms

As stimulated emission is the desired process for lasers light emission, there must be a way to replace the carriers that are being recombined to generate photons, in order to keep the process going. This is obtained by pumping the gain material with an external energy source, i.e. an electrical current.

In order to maximize the probability of carrier recombination and stimulated emission, the active region is sandwiched between p - and n -type cladding layers, forming the so-called Double-Heterostructure (DH). In this structure, the energy gap between conduction and valence band in the cladding material is higher with respect to the one of the active region, so light generated in the active region will not be absorbed in the cladding, as it has a lower energy; in this way, most of the injected carriers recombine in the active region to form photons. Moreover, typically the active region has a higher refractive index with respect to the p - and n - layers, so a dielectric waveguide is formed. By adding mirrors at the ends of the waveguide, it is possible to obtain optical feedback, hence the cavity is formed.

The choice of materials for active region and cladding is not trivial: besides the considerations on the refractive index, the two materials must also have the same crystal structure, in order to epitaxially grow thin defect-free layers of one material over the other. Defects, in fact, cause non-radiative recombinations, i.e. electron-hole recombinations emitting energy in form of heat instead of photons. Non-radiative recombinations must be kept as low as possible, since they reduce the number of the injected carriers that could otherwise give light emission. To make some examples of materials used, in 700-900 μm lasers AlGaAs alloy is grown on GaAs substrate (the cladding). while for long distance lasers InGaAsP/InP systems are used [17].

There are mainly two varieties of diode lasers, the already mentioned VCSELs and the Edge Emitting Lasers (EEL), differing in the way they emit light, as their name suggests. EEL emit light longitudinally to the quantum well, this means that the resonant cavity can be obtained by cleaving the wafer longitudinally to the active region. For VCSEL, instead, mirrors have to be epitaxially grown below and above the quantum well, so that vertical light emission is obtained.

a DBR is essentially a structure made from multiple layers of materials with varying refractive index. Reflectivities higher than 99% can be achieved with a proper design (thickness of each layer must be a quarter of the chosen wavelength) and choice of materials, as reflectivity also depends on the refractive index difference between the high and low index material according to

$$R = \frac{n_1}{n_2} \quad (1.1)$$

Typically, 20-30 layer pairs are used to get high reflectivity, with the lower mirror having more (light should get out mostly from the top aperture). Considering that the active region dimensions are typically in the order of magnitude of λ , it becomes clear that most of the VCSEL volume is dedicated to the mirrors. New techniques are being studied to overcome this problem, like dielectric DBR, offering higher refractive index contrast [18] Qui dire qualcosa sui contatti e sull'apertura

1.2.1 VCSEL vs EEL

1.3 VCSEL in telecommunications

As regards the use of VCSEL in telecom, two major applications can be distinguished, optical transmitters and active optical cables; both targeting short-link (100 to 300 m) data communications and storage area networking (SAN), together they account for the largest market share for VCSELs.

It is possible to list the main features that made VCSELs the predominant choice for optical trasmitters, some of which were already described in 1.2.1:

- low threshold operation;

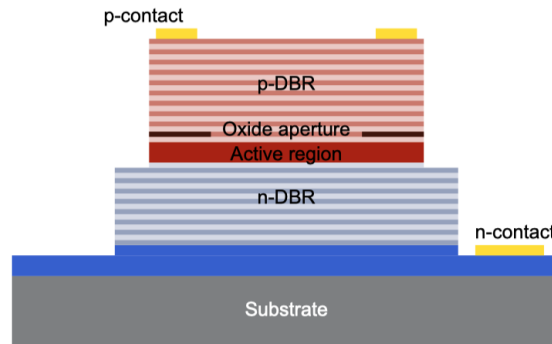
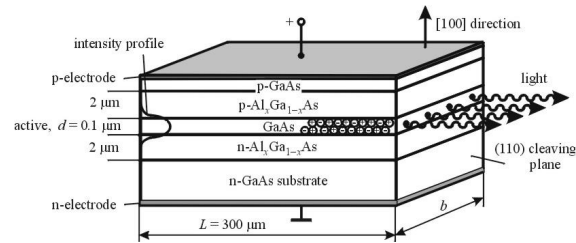
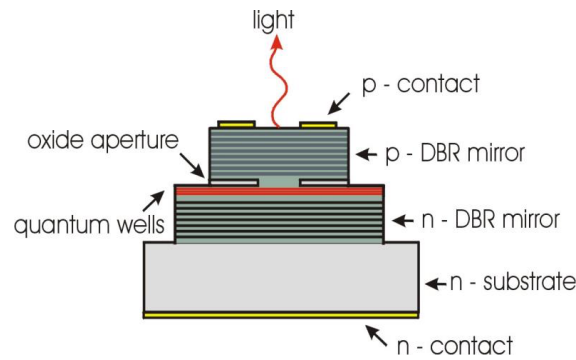


Figure 1.4: Schematic cross-section of a VCSEL [19]



(a) EEL



(b) VCSEL

Figure 1.5: Section of EEL and VCSEL

- relatively small temperature variation impact on wavelength and thresholds;
- high-speed modulation capability;
- long device lifetime;
- high power conversion efficiency (higher than 50 % [21]), defined as the ratio between optical output power and electrical input power;

Edge Emitting Laser (EEL)	VCSEL
Light parallel to quantum well	Light orthogonal to quantum well
Non-circular output beam	Circular output beam
No on-wafer testing	On-wafer testing
Longitudinal multi-mode	Longitudinal single-mode
Larger active volume, leading to higher output power	Smaller active region, lower output power

Table 1.1: Edge Emitting Laser vs VCSEL [20]

- easy coupling to optical fibers due to vertical light emission;
- low cost chip production, since a number of laser devices can be fabricated and tested on a single wafer
- easy bonding and mounting;
- cheap modules and package cost (standardized packages exist, often derived from LED).

Wafer integration also facilitates the creation of VCSEL arrays like the one shown in Figure 1.6b, simplifying the fabrication of parallel optical interfaces to reach higher bitrates. Aforementioned Ethernet standard, provides several examples of parallel solutions, such as 100GBASE-SR4 (10 parallel links at 10 Gbit/s) or 400GBASE-SR16 (16 x 25 Gbit/s), all typically implemented using VCSEL-based transmitters. Besides Ethernet, at least two other standards for data transmission are worth mentioning:

- *Infiniband*, targeting High Performance Computing (HPC) applications [22]
- *Fibre Channel*, an high-speed data transfer protocol mainly addressed to Storage Area Networking (SAN) [23].

1.3.1 State of the art

Most VCSELs today operate at 850 nm wavelength [24] and devices capable of 56 Gbit/s with NRZ modulation are commercially available (e.g. VI-Systems V50-850C).

With the help of electronic equalization, researchers managed to reach 70 Gbit/s at room temperature on commercial devices [25]. Higher-level amplitude modulation formats can provide higher bitrates in exchange for the need of larger power budgets. Using PAM-4 modulation, 60 Gbit/s operations have been demonstrated [26], while with the help of DSP techniques at receiver 112 Gbit/s transmission over

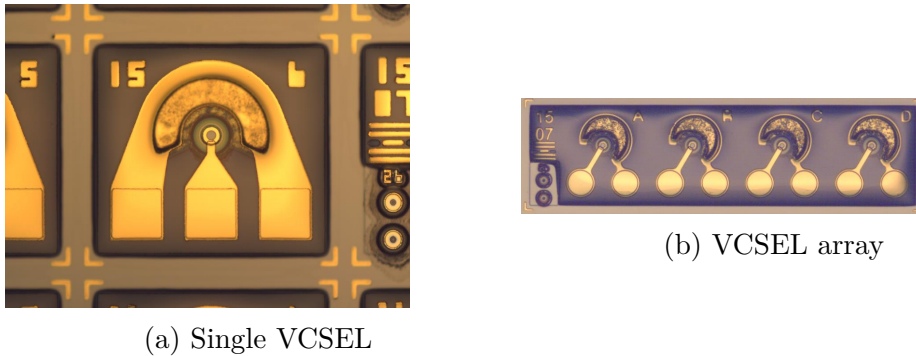


Figure 1.6: VCSEL configurations

100 m has been obtained [27]. Recently, researchers have been moving to higher wavelengths, particularly the 980-1060 nm wavelength range [28, 29] seem to show new possibilities in this field. The advantage of higher wavelengths is an important reduction in loss and chromatic dispersion of the optical fibers. Moreover, Shorter Wavelength Division Multiplexing (SWDM) becomes feasible: using VCSELs working at different wavelengths, independent data streams are multiplexed on the same fiber. It is basically a shorter-wavelength version of CWDM (Coarse Wavelength Division Multiplexing), with the advantage of using VCSELs as transmitters, thus reducing costs. [30, 31]. Feasibility of 400 Gbit/s and beyond has been demonstrated [32]. Commercial products already exist, for example FINISAR sells a transceiver capable of 100 Gbit/s over 100m (4 x 25 Gbit/s), whose block diagram is shown in Figure 1.7. Future high-speed interconnects will also need to

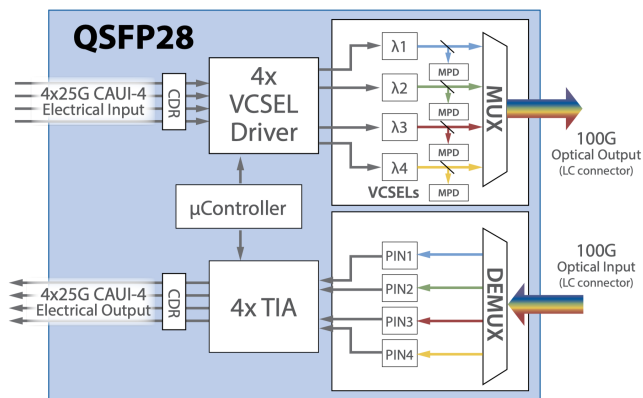


Figure 1: Block Diagram of a 100G SWDM4 QSFP28 Transceiver

Figure 1.7: SWDM4 Transceiver Block Diagram [33]

be extremely energy efficient, both from an economical and environmental point of view: the United States Data Center Energy Usage Report estimates that the

cumulative power usage for US data centers will reach 73 billion kWh in 2020 [34]. Currently deployed VCSEL consume around 25 pJ/bit, most of which used for driver electronics [35], but feasibility of future high-speed interconnect will require the link energy consumption to be dramatically reduced to 1 pJ/bit [36]. Research in this direction has shown promising result, managing to get 100 fJ/bit energy dissipation [37].

1.4 Motivations for this thesis

Given the above, it is evident that numerical simulations have become critical instruments for the analysis and the optimization of high-speed devices and must be able to provide accurate predictions of what will happen in a real scenario. Even though exact characterizations for static and small signal VCSEL behavior [17, 38] exist, the simulation of realistic use-cases such as high bitrate communication systems requires a reliable and, as far as possible, modular numerical toolbox. Several VCSEL simulators have already been proposed in literature [39, 40] while commercial products are available on the market, including LaserMOD [41] from Synopsys and PICS3D [42] from Crosslight Software.

Anyway, the choice of creating a model "from the ground up" has several advantages: it allows both to obtain an adequate understanding about the theoretical concepts on which VCSELs are based and, based on that, to establish the limitations and the potentialities of the simulated model.

1.4.1 Thesis outline - WORK IN PROGRESS

Chapter 2 introduces the theoretical model on which the simulator is based, starting from two rate equations that describe the interaction between photons and carriers. Static and dynamic characteristics are then simulated (PI curve, Small Signal modulation and Relative Intensity Noise), also analyzing the effect of parasitics on the device performances. After that, a relatively simple digital modulation chain is implemented, using the VCSEL as an optical transmitter; Chapter 3 describes the various blocks of the chain and the performance obtained using binary (PAM-2) and multi-level (PAM-4) modulation. Chapter 4 reports laboratory measurements done on VCSELs. Setup and results are discussed for DC characteristics, electrical S-parameters and power spectra. In the end, Chapter 5 draws the conclusions and draws the path for future improvements and works.

Chapter 2

VCSEL modelling

After the short description of the VCSEL "main ingredients" in Chapter 1, it becomes clear that a complete simulation of the VCSEL behavior is not an easy task, as it is at the same time an electrical and optical device. The two fields cannot be treated separately, as light emission is the result of the interplay between electrical and optical phenomena. This simulator, addressing mainly large-signal modulation applications, takes into account some compromises in order to maintain reasonable execution times but at the same time obtain realistic simulation results.

The model used only describes the rates of change of carriers and photons in the active region; moreover, the spatial dependency of these variables is removed, considering constant densities over the active region volume. In reality, the photon density varies spatially as the square of the optical mode field due to the waveguiding of the cavity, which causes the stimulated emission rate to vary accordingly [38]. The spatial nonuniformity of the stimulated emission rate results in an overdamping of the relaxation resonance frequency, which reduces the bandwidth [43]. In real devices, thermal effects play a fundamental role, as most of the parameters that will be described in the following are temperature-dependent and impact on the VCSEL behavior in several ways, some of which are discussed in the following. At least the initial versions of the simulator do not consider thermal effects and this must be kept really clear in mind when discussing the simulation results. Having done all these premises, the interaction between carriers and photons in a single mode VCSEL can now be approximated ([17]) using a system of two rate equations

$$\frac{dN}{dt} = \eta_i \frac{I_{in}}{qV} - (AN + BN^2 + CN^3) - v_{gg}N_p \quad (2.1)$$

$$\frac{dN_p}{dt} = \Gamma v_{gg}N_p + \Gamma\beta BN^2 - \frac{N_p}{\tau_p} \quad (2.2)$$

describing, respectively, the variation of carrier (N) and photon (N_p) density over time.

In Equation 2.1, a generation and two recombination terms can be distinguished:

- $\eta_i I_{in}/qV$ represents carriers generated by the input current; here
 - η_i is the injection efficiency, that is the fraction of input current that generates carriers;
 - I_{in} is the input current;
 - q is the elementary charge;
 - V is the volume of the active region.
- the second term, $AN + BN^2 + CN^3$, includes spontaneous and nonradiative carrier recombinations, where
 - A is the non-radiative recombination term;
 - B is the radiative bimolecular recombination term;
 - C is the Auger non-radiative recombination term.
- $v_g g N_p$ is the stimulated recombination term, where
 - v_g is the group velocity
 - g is the optical gain
 - N_p is the photon density.

In Equation 2.2 photon density increase is accounted through

- the spontaneous emission term $\Gamma\beta BN^2$, in which Γ is the confinement factor and β is the spontaneous emission factor.
- the stimulated emission term $\Gamma v_g g N_p$,

The presence of Γ in the first two terms is explained by the fact that, as the volume occupied by photons (V_p) is usually larger than the one occupied by carriers (the active region), the resulting photon generation will be proportional to $\Gamma = V/V_p$. The β factor, instead, indicates the fraction of the total spontaneous emission going into lasing mode.

The last term in 2.2, N_p/τ_p indicates the photon decrease in the cavity through the photon lifetime term τ_p is the photon lifetime, that accounts for mirror and cavity losses.

As already seen in Section 1.2, gain must overcome losses in order to emit coherent light,, thus reaching threshold. It is possible to express the gain necessary for coherent emission by taking Equation (2.2) and assuming steady state conditions ($dN_p/dt = 0$). Assuming that only a small fraction of the spontaneous emission is coupled into the mode (small β) allows to neglect the third term and to obtain

$$\Gamma v_g g_{th} = \frac{1}{\tau_p} \tag{2.3}$$

The term Γg_{th} is the modal gain. It must be noticed that the steady-state gain for a laser above threshold is equal to the threshold value (i.e. $g(I > I_{th}) = g_{th}$), otherwise the field amplitude in the cavity would keep increasing, thus violating the steady state assumption. It has been shown that gain is dependent on the carrier density [44], and this relationship can be approximated [17] by using

$$g(N) = g'_0 \ln \frac{(N + N_s)}{(N_{tr} + N_s)} \quad (2.4)$$

, where g'_0 is an empirical gain coefficient, N_{tr} the transparency carrier density (i.e. $g(N = N_{tr}) = 0$) and N_s is a shift term in order to get finite logarithm at $N = 0$. By restricting the attention to positive gains ($g > 0$), a valid approximation can be obtained with just two parameters, using the function

$$g(N) = g_0 \ln \left(\frac{N}{N_{tr}} \right) \quad (2.5)$$

in which g_0 is the gain coefficient and N_{tr} is the transparency carrier density. For this work, Dr. Pierluigi Debernardi provided gain curves [45] that were computed using the VENUS multiphysics simulator [40]. Based on these, parameters of equation 2.5 were extracted using a least square fit. Figure 2.1 shows the comparison between the provided curve and the resulting fit. At high photon densities

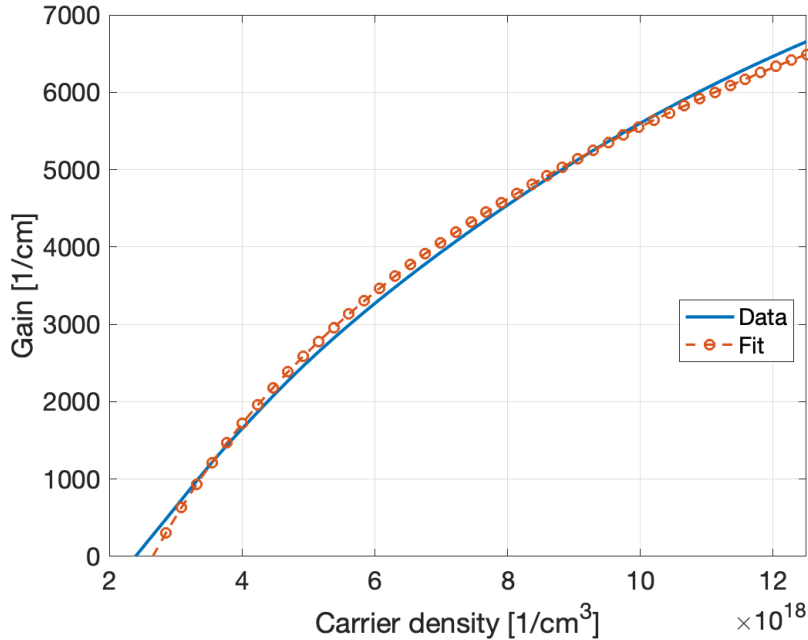


Figure 2.1: Gain fit

gain is compressed due to carrier heating and spectral hole burning ([38]), this can

be taken by rewriting (2.5) as

$$g(N, N_p) = \frac{g(N)}{1 + \epsilon N_p} \quad (2.6)$$

where g is (2.5) gain and ϵ is the gain compression factor.

2.1 Static characteristics

An analytic expression can be constructed to get the output power versus current above threshold. Considering a below threshold situation, in which stimulated emission can be neglected, and assuming steady state condition ($dN/dt = 0$), Equation (2.1) can be rewritten as

$$\frac{\eta_i I}{qV} = \frac{N}{\tau_c} \quad (2.7)$$

that almost at threshold will become

$$\frac{\eta_i I_{th}}{qV} = \frac{N_{th}}{\tau_c} \quad (2.8)$$

By substituting (2.8) in (2.1), it results that

$$\frac{dN}{dt} = \frac{\eta_i(I - I_{th})}{qV} - v_g g N_p \quad (2.9)$$

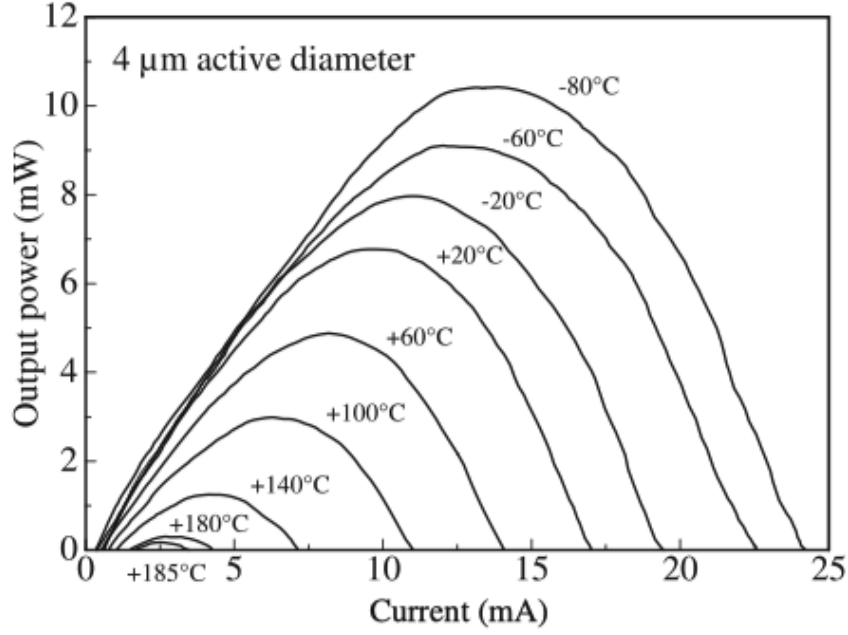
From (2.9) it is now possible to obtain a steady-state photon density as

$$N_p = \frac{\eta_i(I - I_{th})}{qv_g g_{th} V} \quad (2.10)$$

By considering the energy in the cavity, where h is the Planck constant and ν is the VCSEL central frequency, and, the power..., the output power becomes

$$P_{out} = \eta_0 h \nu \frac{N_p V_p}{\tau_p} \quad (2.11)$$

The factor η_0 is the optical efficiency, and it defines the fraction of power that is output from the laser aperture. In Figure 2.2 it is possible to observe a typical PI curve for a VCSEL; curves for different temperatures are shown, so thermal effects are evident, particularly power roll-off, increase of the threshold and decrease in slope efficiency (output power vs. input current).


 Figure 2.2: PI curve of a VCSEL with 4 μm active diameter [46]

The rate equations were solved using the Runge-Kutta 4th Order Method

Parameter	Value	Unit
η_i	0.9	•
η_o	0.52	•
V		cm^3
τ_c	$3.8 * 10^{-9}$	s
B	$7.6 * 10^{-11}$	cm^3/s
C	$1 * 10^{-30}$	cm/s^6
v_g	$9.08 * 10^7$	m/s
g_0		
N_{tr}		cm
ϵ		cm^3
Γ	0.03	•
τ_p	$2.2 * 10^{-12}$	s
β	$1 * 10^{-4}$	•

Table 2.1: List of parameters used in the simulations

After simulating for currents from ... to

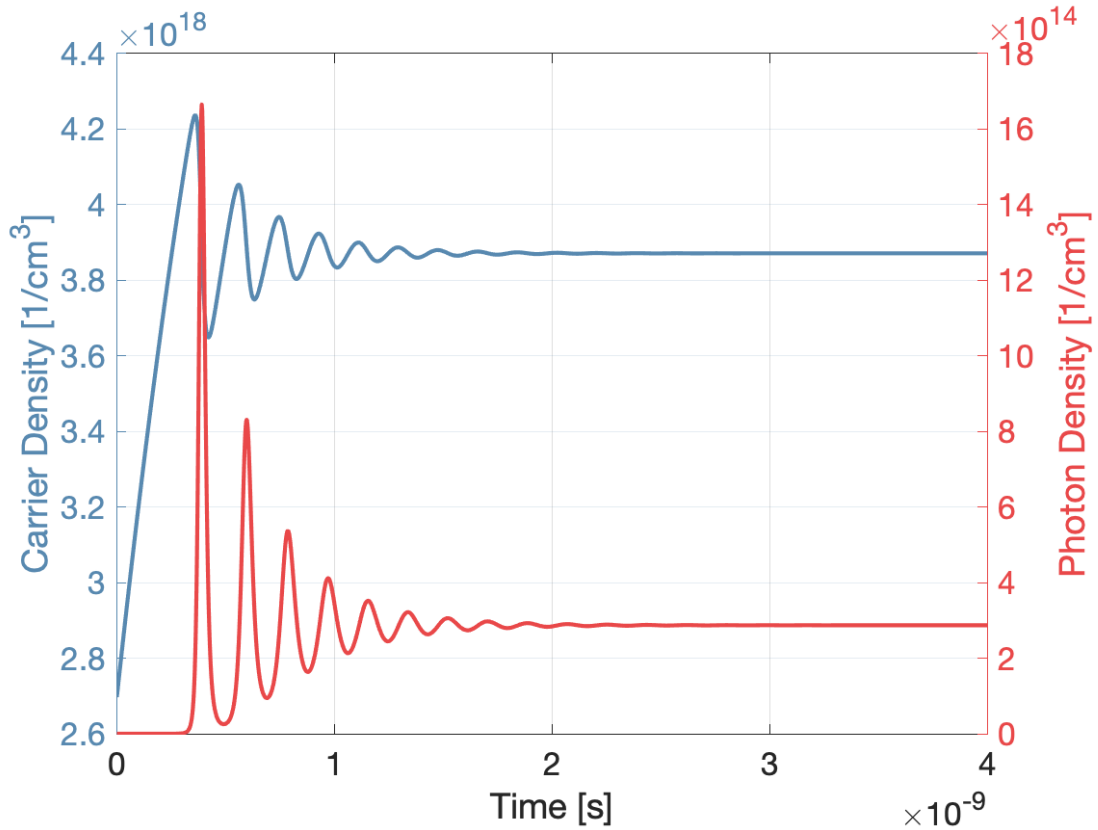


Figure 2.3: Carrier and photon density over time

2.2 Dynamic analysis

Although DC characteristics provide a good measure of the power output capabilities, the simulator aims to describe VCSEL usage as an optical transmitter, that means modulated using large signals. It is therefore important to characterize the dynamic performance of the device and its speed-limiting factors. The first step in this direction is to get a simplified version of the rate equation that output the VCSEL frequency response when it works around a steady-state point. It is to obtain a simplified version of the rate equations that give the response in frequency of the VCSEL that works around a steady-state point. A dynamic analysis of the interaction between photons and carriers requires to analyze time derivatives of the rate equations; no analytical solution exists, anyway some approximations can be made when dynamic changes of N and N_p are small with respect to the

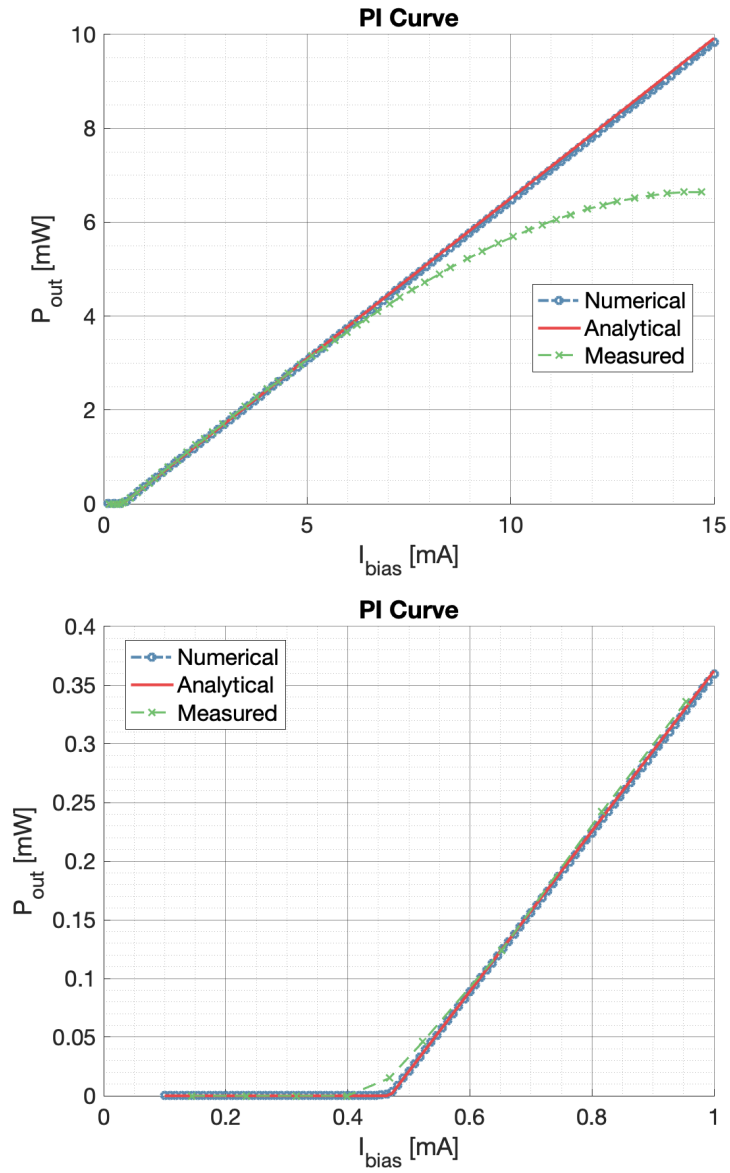


Figure 2.4: aaa

steady-state value, that is

$$N = N_0 + \delta N \quad (2.12)$$

$$N_p = N_{p_0} + \delta N_p \quad (2.13)$$

. where the subscript 0 indicates the steady-state value. Taking the derivatives of Equations 2.1 and 2.2 it is possible to get ([17])

$$d \left[\frac{dN}{dt} \right] = \frac{\eta_i}{qV} dI - \frac{1}{\tau_{\Delta N}} - v_g g dN_p - N_p v_g dg \quad (2.14)$$

$$d \left[\frac{dN_p}{dt} \right] = \left[\Gamma v_g g - \frac{1}{\tau_p} \right] dN_p + N_p \Gamma v_g dg + \frac{\Gamma}{\tau_{\Delta N}} dN \quad (2.15)$$

where

$$\frac{1}{\tau_{\Delta N}} = A + BN^2 + CN^3 \quad \frac{1}{\tau_{\Delta N}'} = 2\beta BN \quad (2.16)$$

Moreover, assuming that gain variation depends by carrier and photon density variations, it is possible to write

$$dg = a dN - a_p dN_p \quad (2.17)$$

where

$$a = \frac{\partial g}{\partial N} = \frac{g_0}{1 + \epsilon N_p} \ln \left(\frac{N}{N_{tr}} \right) \quad a_p = \frac{-\partial g}{\partial N_p} = \frac{\epsilon g}{1 + \epsilon N_p} \quad (2.18)$$

After defining the rate coefficients

$$\gamma_{NN} = \frac{1}{\tau_{\Delta N}} + v_g a N_p, \quad \gamma_{NP} = \frac{1}{\Gamma \tau_p} - \frac{R'_{sp}}{N_p} - v_g a_p N_p \quad (2.19)$$

$$\gamma_{PN} = \frac{\Gamma}{\tau_{\Delta N}'} + \Gamma v_g a N_p, \quad \gamma_{PP} = \frac{\Gamma R'_{sp}}{N_p} + \Gamma v_g a_p N_p \quad (2.20)$$

Equations 2.14 and 2.15 become

$$\frac{d}{dt} (dN) = \frac{\eta_i}{qV} dI - \gamma_{NN} dN - \gamma_{NP} dN_p \quad (2.21)$$

$$\frac{d}{dt} (dN_p) = \gamma_{PN} dN - \gamma_{PP} dN_p \quad (2.22)$$

The previous definition of the rate coefficients 2.19 allows to write the differential rate equations in a matrix form,

$$\frac{d}{dt} \begin{bmatrix} dN \\ dN_p \end{bmatrix} = \begin{bmatrix} -\gamma_{NN} & -\gamma_{NP} \\ \gamma_{PN} & -\gamma_{PP} \end{bmatrix} \begin{bmatrix} dN \\ dN_p \end{bmatrix} + \frac{\eta_i}{qV} \begin{bmatrix} dI \\ 0 \end{bmatrix} \quad (2.23)$$

Equation (2.23) is useful since the VCSEL response is expressed in terms of a forcing term, that in this case is the current. This formulation will be useful in the modelling of noise where, instead of the current term, two noise sources will be used, one for carriers and one for photons.

2.3 Small Signal Frequency Response

Let's consider the application of a small sinusoidal current over the bias term I_0 , such that $I_1 \ll I_0$ with I_1 being the amplitude of the AC signal. The resulting carrier and photon densities should vary accordingly. By writing the derivatives in complex frequency notations,

$$dI(t) = I_1 e^{j\omega t} \quad (2.24)$$

$$dN(t) = N_1 e^{j\omega t} \quad (2.25)$$

$$dN_p(t) = N_{p1} e^{j\omega t} \quad (2.26)$$

Setting $d/dt = j\omega$, Eq. (2.23) can be rearranged as

$$\begin{bmatrix} \gamma_{NN} + j\omega & \gamma_{NP} \\ -\gamma_{PN} & \gamma_{PP} + j\omega \end{bmatrix} \begin{bmatrix} N_1 \\ N_{p1} \end{bmatrix} = \frac{\eta_i I_1}{qV} \begin{bmatrix} 1 \\ 0 \end{bmatrix} \quad (2.27)$$

The small signal carrier and photon densities can now be obtained by using the Cramer's rule

$$N_1 = \frac{\eta_i I_1}{qV} \frac{1}{\Delta} \begin{vmatrix} 1 & \gamma_{NP} \\ 0 & \gamma_{PP} + j\omega \end{vmatrix} \quad (2.28)$$

$$N_{p1} = \frac{\eta_i I_1}{qV} \frac{1}{\Delta} \begin{vmatrix} \gamma_{NN} + j\omega & 1 \\ -\gamma_{PN} & 0 \end{vmatrix} \quad (2.29)$$

$$(2.30)$$

where Δ is the determinant of the leftmost matrix in (2.27)

$$\Delta = \begin{vmatrix} \gamma_{NN} + j\omega & \gamma_{NP} \\ -\gamma_{PN} & \gamma_{PP} + j\omega \end{vmatrix} \quad (2.31)$$

$$= \gamma_{NP}\gamma_{PN} - \omega^2 + j\omega(\gamma_{NN} + \gamma_{PP}) \quad (2.32)$$

After the expansion of the determinant, the small signal solutions will be

$$N_1 = \frac{\eta_i I_1}{qV} \cdot \frac{\gamma_{PP} + j\omega}{\omega_R^2} H(\omega) \quad (2.33)$$

$$N_{p1} = \frac{\eta_i I_1}{qV} \cdot \frac{\gamma_{PN}}{\omega_R^2} H(\omega) \quad (2.34)$$

where the modulation response is expressed in terms of the modulation transfer function

$$H(\omega) = \frac{\omega_R^2}{\omega_R^2 - \omega^2 + j\omega\gamma} \quad (2.35)$$

Here ω_R is the relaxation frequency and γ is the damping factor, and can be associated to the previous parameters as

$$\omega_R^2 \equiv \gamma_{NP}\gamma_{PN} + \gamma_{NN}\gamma_{PP} \quad (2.36)$$

$$\gamma \equiv \gamma_{NN} + \gamma_{PP} \quad (2.37)$$

Basically, the VCSEL small signal frequency response is that of a second order low-pass filter, and an example is shown in Figure 2.5.

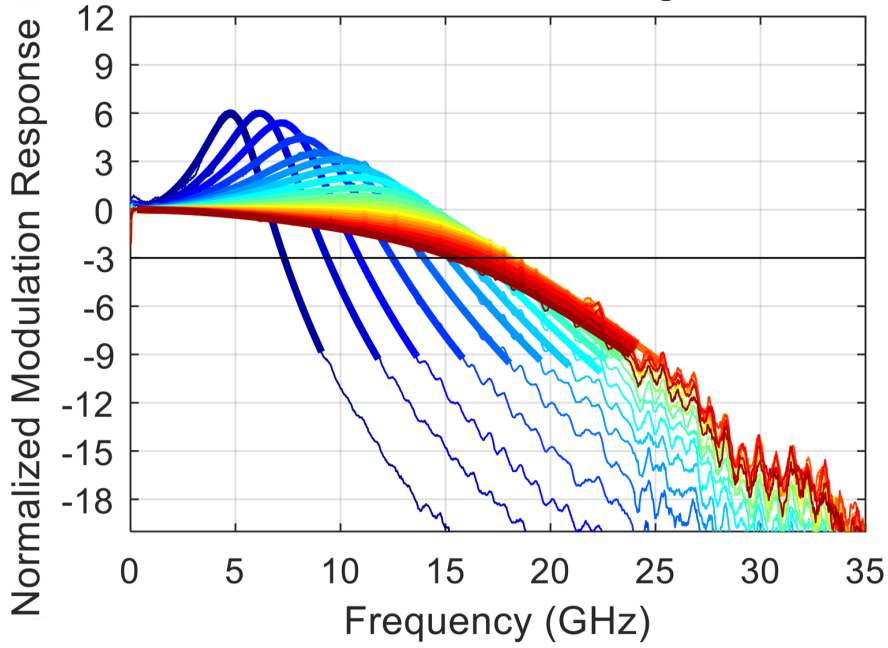


Figure 2.5: Small signal modulation response for a real device at different currents

By expanding the rate coefficients according to 2.19, the two parameters characterizing the transfer function can be rewritten as

$$\omega_R^2 = \frac{v_g a N_p}{\tau_p} + \left[\frac{\Gamma v_g a_p N_p}{\tau_{\Delta N}} + \frac{\Gamma R'_{sp}}{N_p \tau_{\Delta N}} \right] \left(1 - \frac{\tau_{\Delta N}}{\tau'_{\Delta N}} \right) + \frac{1}{\tau'_{\Delta N} \tau_p} \quad (2.38)$$

$$\gamma = v_g a N_p \left[1 + \frac{\Gamma a_p}{a} \right] + \frac{1}{\tau_{\Delta N}} + \frac{\Gamma R'_{sp}}{N_p} \quad (2.39)$$

$$\gamma = K f_r^2 + \gamma_0 \quad (2.40)$$

where

$$K = 4\pi^2 \tau_p \left[1 + \frac{\Gamma a_p}{a} \right] \quad (2.41)$$

and

$$\gamma_0 = \frac{1}{\tau_{\Delta N}} + \frac{\Gamma R_{sp}'}{N_p}. \quad (2.42)$$

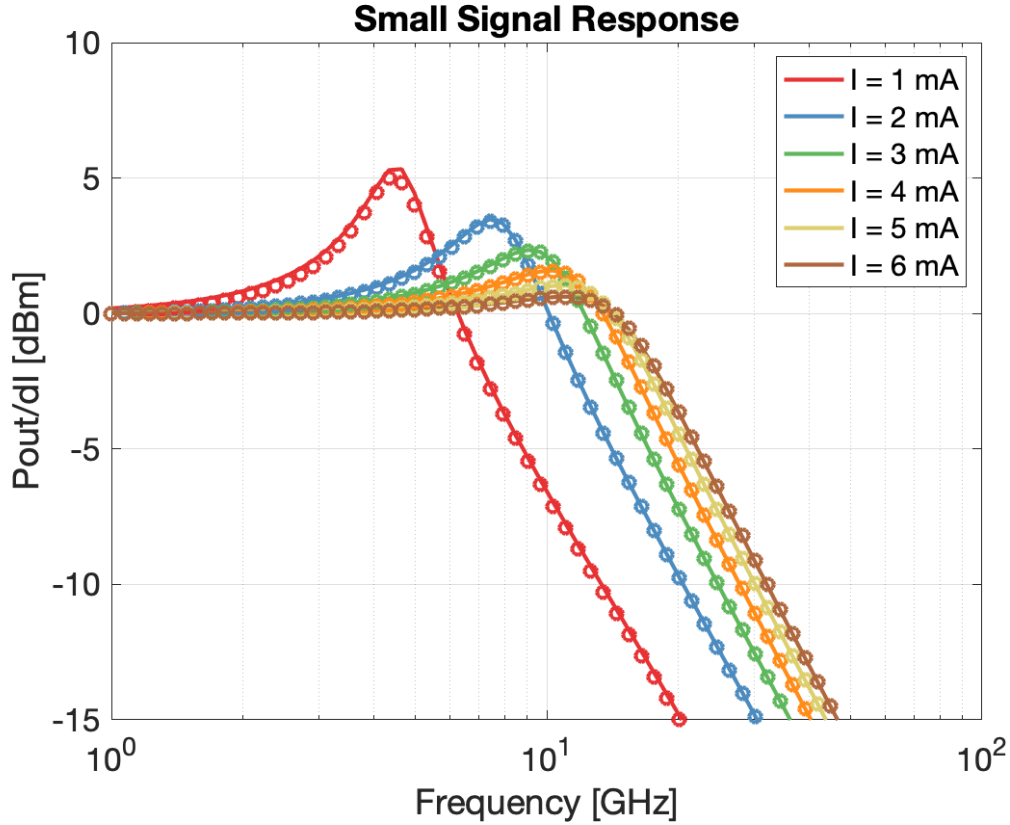


Figure 2.6: Simulated Small Signal Response. Dots represent the simulation output, while full line is the analytical curve

Even after fitting the simulation output to the measured data, there is still some mismatch between the two curves. One possible explanation is the presence of parasitics in the VCSEL structure, described in the next section.

2.4 Some hints on parasitics

The design and manufacturing of high-frequency devices must pay great attention to parasitics, as they will inevitably limit the modulation bandwidth. In most cases, it is desirable to minimize the parasitics in order to go as close as possible to the intrinsic bandwidth.

A possible model describing VCSEL parasitics is the equivalent circuit shown in Figure 2.7. In this circuit:

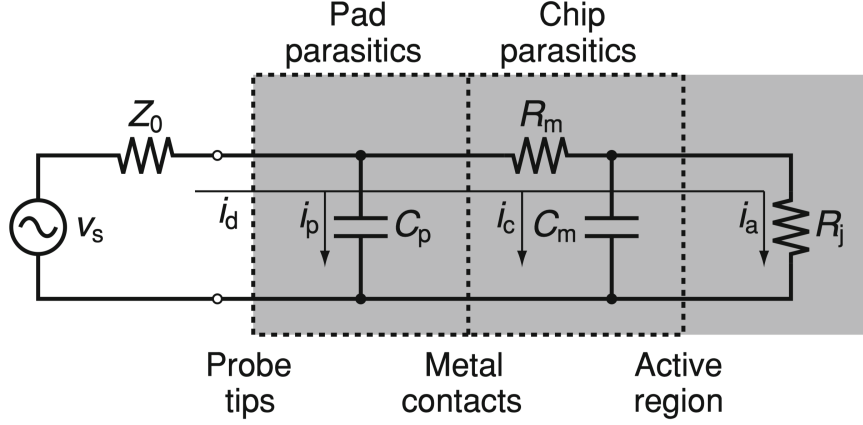


Figure 2.7: Small signal model including driving source - the grey area represents the VCSEL [38]

- V_s and Z_0 are the driver voltage and its characteristic impedance
- C_p is the pad capacitance
- C_m is a combination of the oxide layer and the active region capacitances
- R_m is the mirror resistance
- R_j is the junction resistance, representing the intrinsic laser

The driving current i_d , due to the various effects listed above, is diverted from entering the laser due to i_p and i_c . The resulting effect on the modulation can be described through a transfer function from the voltage source to the current flowing to the intrinsic laser

$$H_{ext}(\omega) = \frac{i_a \omega}{v_s} \quad (2.43)$$

and can be approximated as a single-pole low-pass filter

$$H_{ext}(\omega) = \frac{1}{1 + j\omega/\omega_0} \quad (2.44)$$

where ω_0 is the parasitic roll-off frequency. The overall frequency response can now be written as

$$H(\omega) = \frac{P_{out}}{V_s} \quad (2.45)$$

$$= H_{ext}(\omega)H_{int}(\omega) \quad (2.46)$$

$$\propto \left(\frac{1}{1 + j(\omega/\omega_0)} \frac{\omega^2}{(\omega_r^2 - \omega^2)^2 + j\omega\gamma} \right) \quad (2.47)$$

where $H_{int}(\omega)$ is the intrinsic VCSEL response (Equation 2.35). The input impedance of the VCSEL can be expressed as

$$Z_{VCSEL} = \left(j2\pi C_p + \left(\frac{R_j}{1 + j2\pi f C_a R_j} + R_m \right)^{-1} \right)^{-1} \quad (2.48)$$

When measured electrical parameters are available, it is possible to fit the S_{11} curve to the VCSEL impedance through

$$S_{11} = \frac{Z_{VCSEL} - Z_0}{Z_{VCSEL} + Z_0} \quad (2.49)$$

and from there find the circuit parameters.

Going back to the previous curves, it turns out that a good fit is obtained setting $f_0 = 22$ GHz, even though a perfect match is still not obtained (Figure 2.8).

This can be due to the model chosen to describe the parasitics (Figure 2.7) that neglects possible inductive effects in the device [38]. Future work on the simulator could address this problem by using a more complex equivalent fit, like the one described in [10]. The effects of adding the single pole filter to the overall transfer function are shown in Figure 2.9.

2.5 Noise Analysis

Up to now, the assumption was that the output responses were only caused by the input current, so that in the steady state carrier and photon densities remained constant. In real devices, even when no current is applied, there are spontaneous random generations and recombinations of photons and carriers; these phenomena must be taken into account in the model, as variation in photon density cause fluctuations in the output power. A useful quantifier of this effect is the Relative Intensity Noise (RIN) of the VCSEL, expressed as

$$RIN \equiv \frac{\langle \delta P(t)^2 \rangle}{P_0^2} \quad (2.50)$$

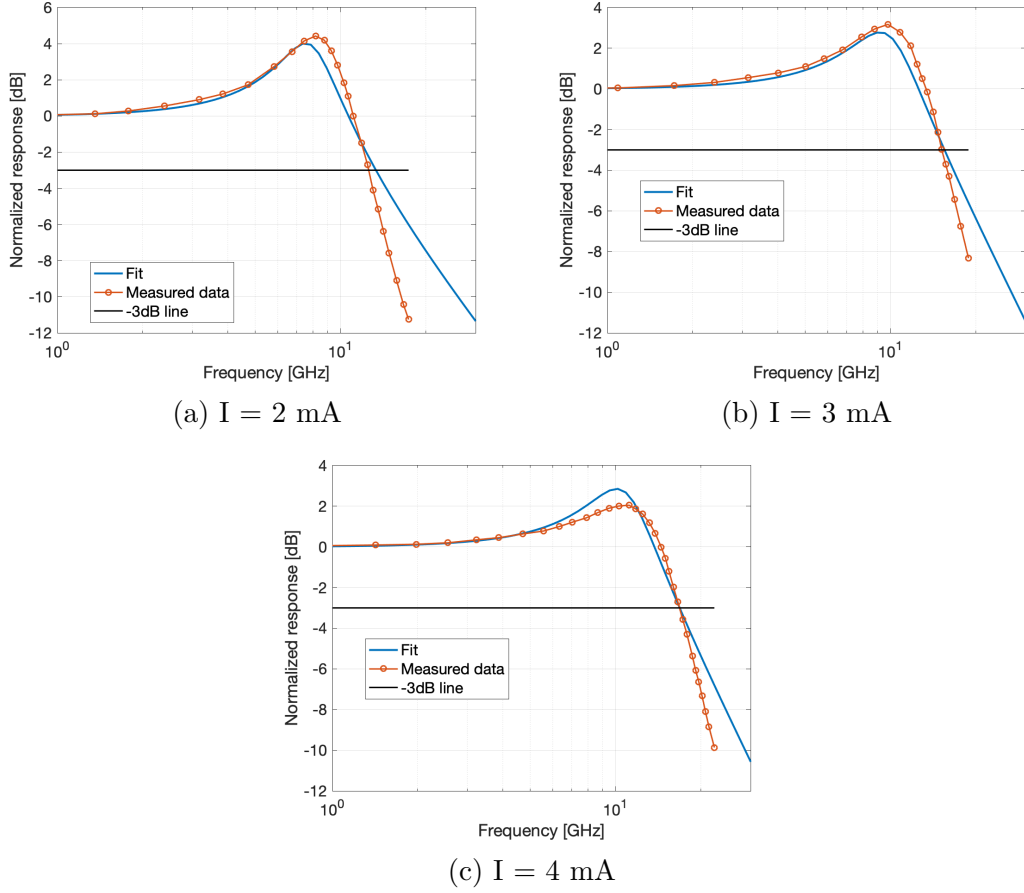


Figure 2.8: Filtered small signal response vs. measured curve

The numerator of the fraction (describing output power fluctuations) can be easily described in the frequency domain, in fact using

$$\delta P(\omega) = \int_{-\infty}^{+\infty} \delta P(t) e^{-j\omega t} dt \quad (2.51)$$

it is possible to write

$$\langle \delta P(t)^2 \rangle = \frac{1}{(2\pi)^2} \int_{-\infty}^{+\infty} \int_{-\infty}^{+\infty} \langle \delta P(\omega) \delta P(\omega')^* \rangle F(\omega) F(\omega')^* e^{j(\omega - \omega')t} d\omega d\omega' \quad (2.52)$$

where $F(\omega)$ is the filter used to analyze the signal. Assuming completely random noise,

$$\langle \delta P(\omega) \delta P(\omega')^* \rangle = S_{\delta P}(\omega) 2\pi \delta(\omega - \omega') \quad (2.53)$$

. Using 2.53, after some substitutions (2.52) becomes

$$\langle \delta P(t)^2 \rangle \approx S_{\delta P}(\omega_0) 2\Delta f \quad (2.54)$$

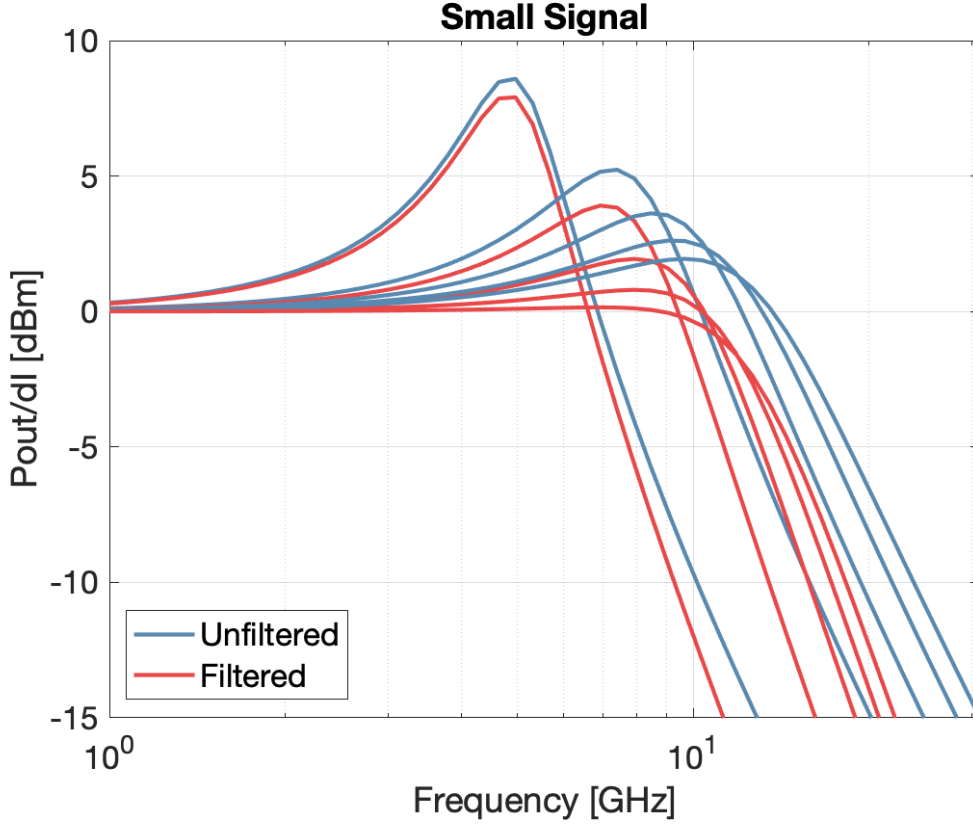


Figure 2.9: Small Signal Response - comparison after adding parasitics

RIN can be then rewritten in terms of spectral density of the noise as

$$\frac{RIN}{\Delta f} = \frac{2S_{\delta P}(\omega)}{P_0^2}, \quad (2.55)$$

that is the RIN per unit bandwidth. Full RIN is found by integrating (2.55) over the bandwidth of interest.

To find fluctuations in the output power spectral density, two white noise sources, $F_N(t)$ and $F_P(t)$, are used. Assuming F_N and F_P small enough (in order to use differential rate equations) and $dI = 0$ (constant drive current), equation 2.23 becomes

$$\frac{d}{dt} \begin{bmatrix} dN \\ dN_p \end{bmatrix} = \begin{bmatrix} -\gamma_{NN} & -\gamma_{NP} \\ \gamma_{PN} & -\gamma_{PP} \end{bmatrix} \begin{bmatrix} dN \\ dN_p \end{bmatrix} + \begin{bmatrix} F_N(t) \\ F_P(t) \end{bmatrix} \quad (2.56)$$

By rewriting the previous equation in the frequency domain, according to ,

$$\begin{bmatrix} \gamma_{NN} + j\omega & \gamma_{NP} \\ -\gamma_{PN} & \gamma_{PP} + j\omega \end{bmatrix} \begin{bmatrix} N_1 \\ N_{p1} \end{bmatrix} = \frac{\eta_i I_1}{qV} \begin{bmatrix} F_N(\omega) \\ F_P(\omega) \end{bmatrix} \quad (2.57)$$

Now N_1, N_{p1}, F_N and F_P are the noise component fluctuating at frequency ω . The interest here is in finding the spectral density of both carrier and photons, i.e.

$$S_N(\omega) = \frac{1}{2\pi} \int \langle N_1(\omega) N_1(\omega')^* \rangle d\omega',$$

$$S_{N_p}(\omega) = \frac{1}{2\pi} \int \langle N_{P1}(\omega) N_{P1}(\omega')^* \rangle d\omega'$$

After some calculations, one finds

$$S_N(\omega) = \frac{|H(\omega)|^2}{\omega_R^4} \left[\gamma_{NP}^2 \langle F_P F_P \rangle - 2\gamma_{PP}\gamma_{NP} \langle F_P F_N \rangle + (\gamma_{PP}^2 + \omega^2) \langle F_N F_N \rangle \right] \quad (2.58)$$

$$S_{N_p}(\omega) = \frac{|H(\omega)|^2}{\omega_R^4} \left[(\gamma_{NN}^2 + \omega^2) \langle F_P F_P \rangle + 2\gamma_{NN}\gamma_{PN} \langle F_P F_N \rangle + \gamma_{PN}^2 \langle F_N F_N \rangle \right] \quad (2.59)$$

In Equations 2.58 and 2.59, the terms $\langle F_i F_j \rangle$ are the Langevin noise source spectral densities. It can be shown ([17, Appendix 14]) that if $N_p V_p \gg 1$ these terms reduce to

$$\langle F_P F_P \rangle = 2\Gamma R'_{sp} N_p \quad (2.60)$$

$$\langle F_N F_N \rangle = 2R'_{sp} N_p / \Gamma - v_g g N_p / V + \eta_i (I + I_{th}) / qV^2 \quad (2.61)$$

$$\langle F_P F_N \rangle = -2R'_{sp} N_p + v_g g N_p / V_p \quad (2.62)$$

Power spectral density above threshold can be expressed as

$$S_{\delta P}(\omega) = h\nu P_0 \left[\frac{a_1 + a_2 \omega^2}{\omega_R^4} |H(\omega)|^2 + 1 \right] \quad (2.63)$$

where

$$a_1 = \frac{8\pi(\Delta\nu)_{ST} P_0}{h\nu} \frac{1}{\tau_{\Delta N}^2} + \eta_0 \omega_R^4 \left[\frac{\eta_i (I + I_{th})}{I_{st}} - 1 \right]$$

$$a_2 = \frac{8\pi(\Delta\nu)_{ST} P_0}{h\nu} - 2\eta_0 \omega_R^2 \frac{\Gamma a_p}{a}$$

Finally

$$\frac{RIN}{\Delta f} = \frac{2h\nu}{P_0} \left[\frac{a_1 + a_2 \omega^2}{\omega_R^4} |H(\omega)|^2 \right] \quad (2.64)$$

2.6 Conclusions

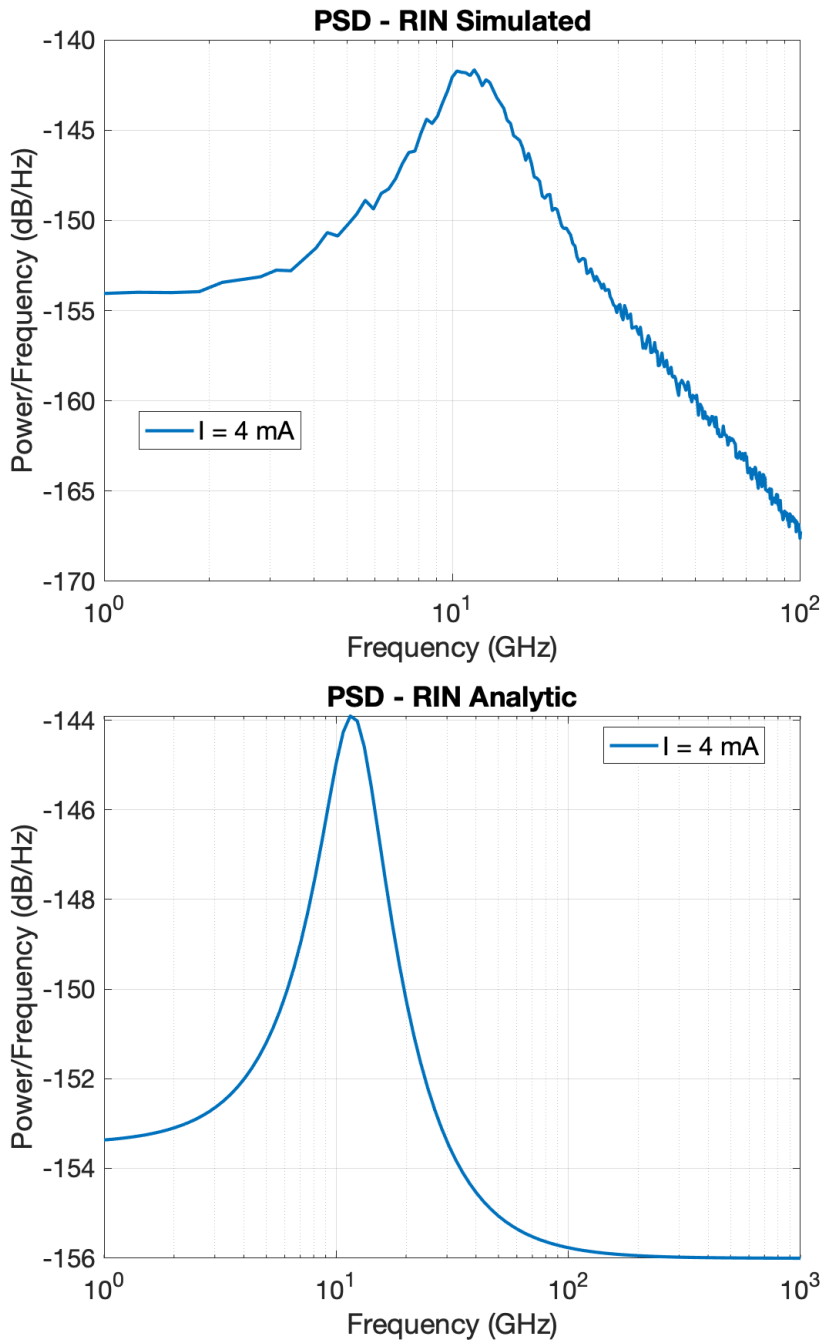


Figure 2.10: RIN

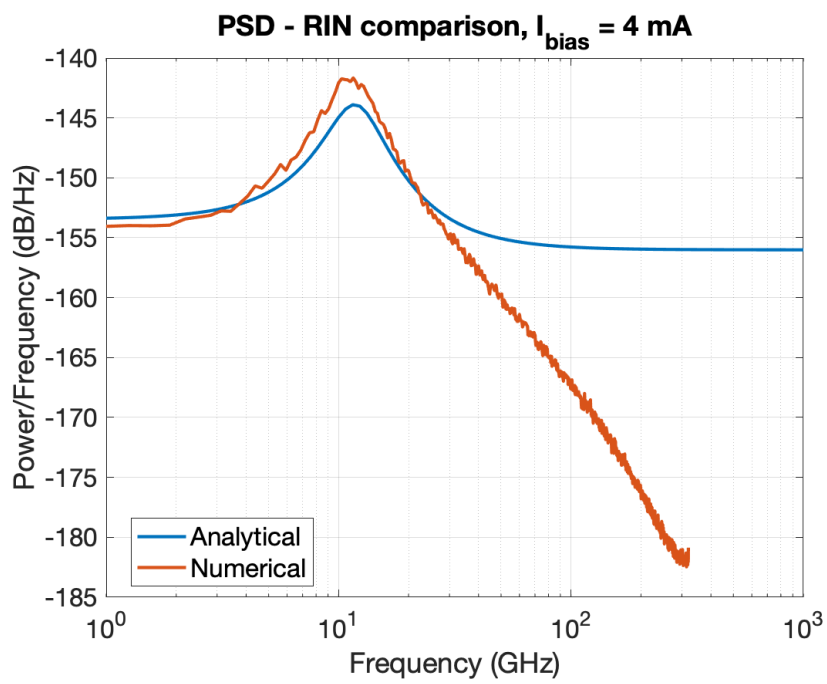


Figure 2.11: Analytical RIN vs. rate equations

Chapter 3

Large signal modulation

In Chapter 2 it was proven that the numerical simulator shows both outputs corresponding to the expected (analytical) ones and similar characteristics (up to some extent) as a real one. As already stated, VCSEL-based optical communication systems work under large-signal modulations. So the following step was the implementation of a large signal modulation system.

Short-range optical interconnects typically implement Intensity Modulation/Direct Detection (IM/DD) schemes to transmit informations. The term Intensity Modulation refers to the transmitter, where the information bits are encoded as instantaneous current level variations that a VCSEL transforms into variable output power, to be sent on the fiber. As regards the receiver, here a photodiode converts the received power directly to an electrical signal (hence, Direct Detection), that is then amplified, low-pass filtered and sampled. The received samples, at this point, are input to a decision circuit that implements decision by threshold. In Figure 3.1, the main components of an IM/DD systems are highlighted

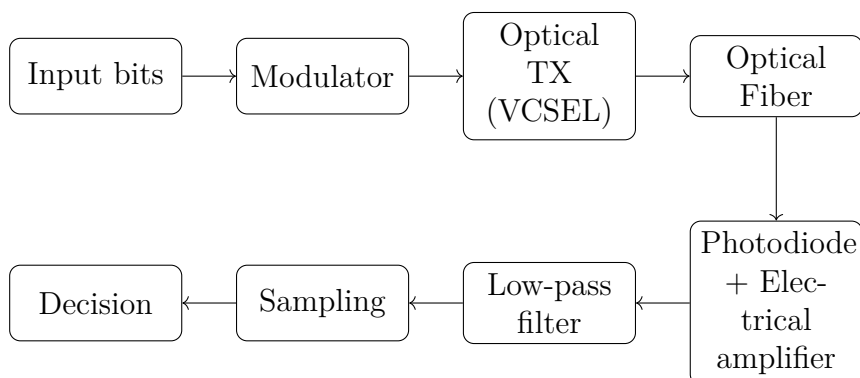


Figure 3.1: Block diagram of the implemented modulation scheme

In the simulator, a simplified version of an IM/DD system was implemented, shown in Figure 3.2. The starting point is the generation of sequences of bits called



Figure 3.2: Block diagram of the implemented modulation scheme

Pseudo-Random Binary Sequences (PRBS). The peculiarity of these sequences is that they have statistical characteristic that make them "look like" real random sequences. Zeros and ones are then modulated using chosen current levels. At this point, attention must be paid: since the implemented model does not include thermal effects, the current levels must be chosen with care. The VCSEL described by the parameters used in the simulation will have power roll-off above a given level of input current, which will not be considered by the simulation. This means that if currents levels are selected in the roll-off region, the simulator will provide results that are incongruous with a real scenario.

At this point the simulated input current is practically a piecewise constant function with two values (the two current levels chosen), but with vertical transitions from one level to another. In a real scenario, this would have no physical meaning since that would imply zero rise and fall time in the real modulated current. This is of course impossible, and to avoid it the signal must be filtered. For this purpose, a Gaussian filter was used, since it can be easily implemented in software and it can be proven that it has no overshoot for a step function input. Its input response can be written as

$$h_{gauss}(t) = \frac{1}{\sqrt{2\pi\sigma^2}} e^{\left(\frac{-t^2}{2\sigma^2}\right)} \quad (3.1)$$

where $\sigma = \sqrt{\ln(2)}/2\pi BT$, in which B is the 3 dB bandwidth (one-sided) of the Gaussian filter and T is the bit period [47]. In order to maintain modularity in the simulator and allow attempts at different bitrates, the bandwidth of the filter was set as $B = T/3$.

Now the current is ready to be input to the VCSEL, whose output power is obtained, again, by numerically solving the rate equations. From Figure 3.1 the subsequent blocks should be the optical fiber followed by the photodiode, anyway the choice was to only consider the receiver filter, in order to check the effect of RIN on the received signal. It was implemented as a 4th order Bessel Filter, with a cutoff frequency of $0.7 R$, where R is the simulation bitrate.

After having introduced the complete implemented scheme, results for PAM-2 and PAM-4 modulation are reported.

3.1 PAM-2 (NRZ) modulation

One of the simplest modulation format is the two-level pulse amplitude modulation (PAM-2), where ones and zeros are represented by two current levels. Here, the low-level bias I_0 was set to 2 mA, in order to work above threshold and so to avoid turn-on delays in the VCSEL, while the high-level current I_1 , instead, was set to 6 mA to avoid roll-off effects, as explained before. Figure 3.3 shows the implemented PAM-2 scheme.



Figure 3.3: Binary modulation scheme - block diagram

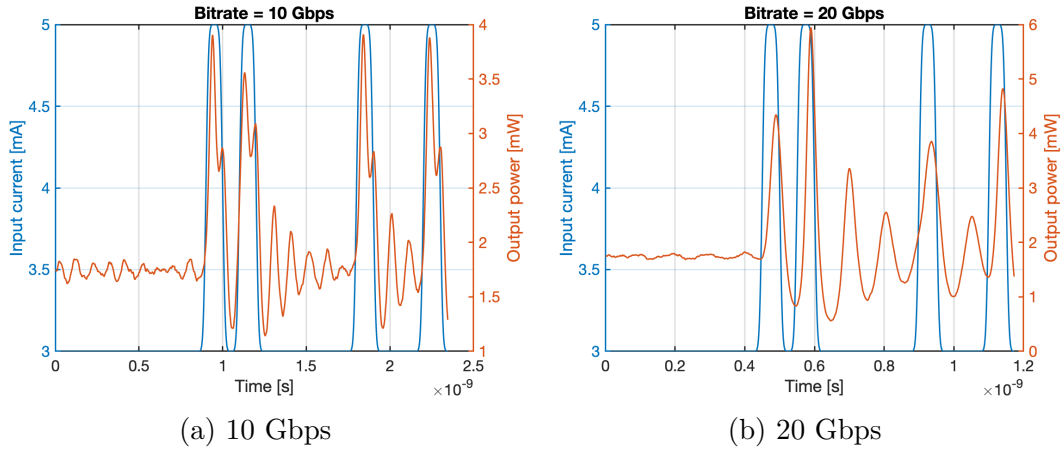


Figure 3.4: PAM-2 - Modulation current and resulting output power

Figure 3.4 shows the VCSEL power output superimposed to the modulated input current.

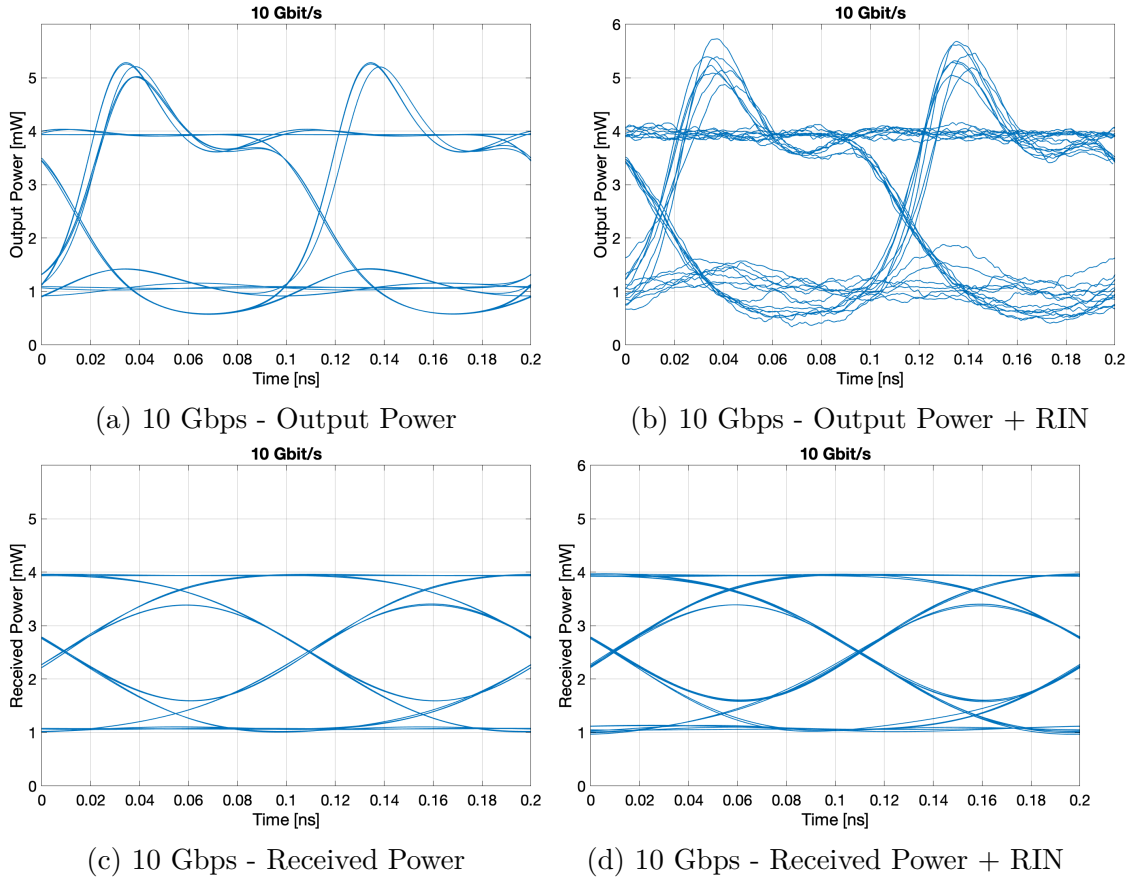


Figure 3.5: PAM-2 - Effects of RIN at 10 Gbps

An attempt of modulation at 30 Gbps was done, with the results shown in Figures 3.7a and 3.7b. The eye diagram of the VCSEL output power shows a very noisy situation, in which the relaxation oscillation of the VCSEL seem to occupy the entire bit period. This was expected by looking at the small signal response, that indicated a 3dB bandwidth of around 19 GHz at 6 mA. To make things worse, the other eye diagram seems to indicate that the receiver filter adds further intersymbolic interference.

3.1 – PAM-2 (NRZ) modulation

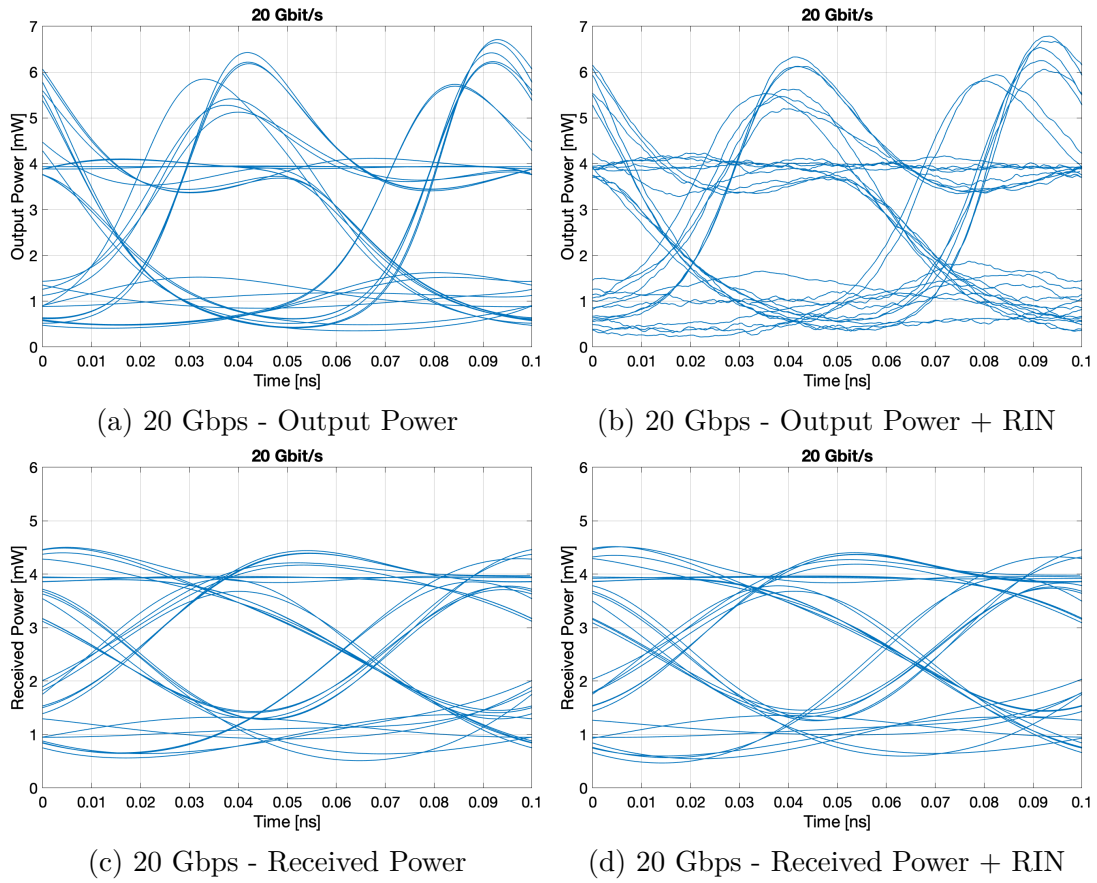


Figure 3.6: PAM-2 - Effects of RIN at 20 Gbps

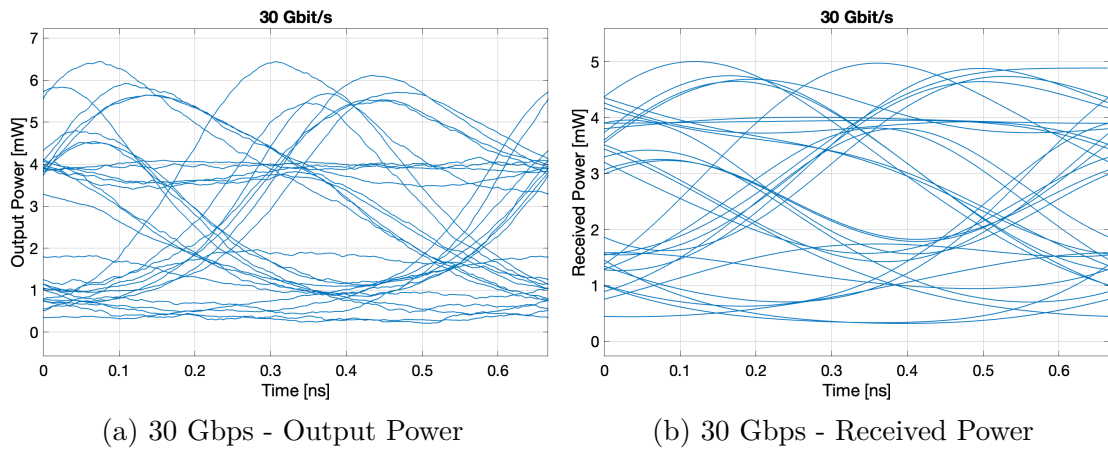


Figure 3.7: PAM-2 modulation - attempts at 30 Gbps

3.2 PAM-4 modulation

The advantage of using a four-level modulation derives from the fact that it doubles the spectral efficiency (defined as the information rate transmitted over a given bandwidth). The price to pay is a higher signal to noise ratio (SNR) needed to obtain the same performance. In order to obtain four levels, the input bit sequence is divided into 2-bits long symbols. Consequently, four levels of currents must be used. Again, 2 and 6 mA are used as lowest and highest bias levels, but this time two equispaced current levels in this range are used, as shown in Table 3.1.



Figure 3.8: PAM-4 - block diagram

Symbol	Bias current
00	2 mA
01	3.33 mA
10	4.66 mA
11	6 mA

Table 3.1: PAM-4 bias currents

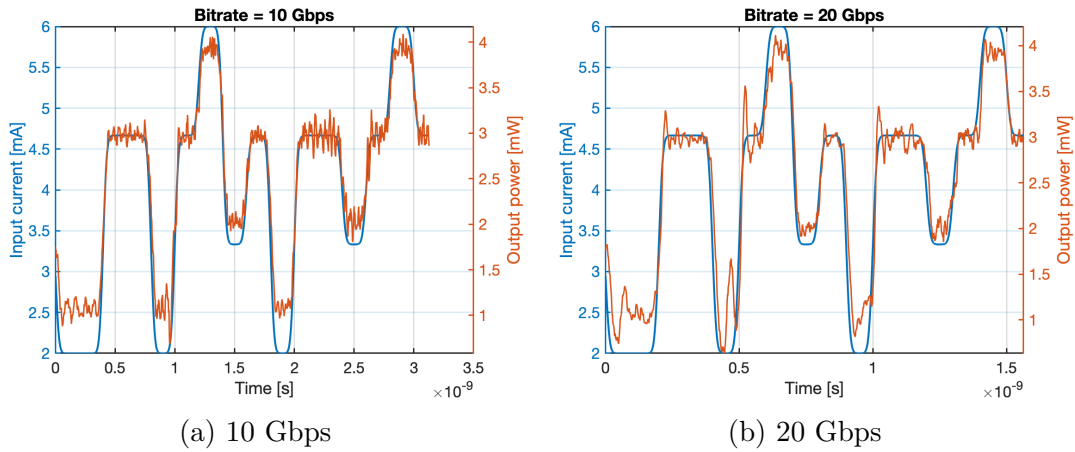
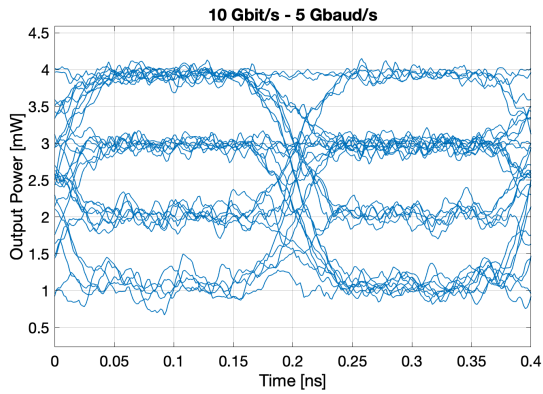
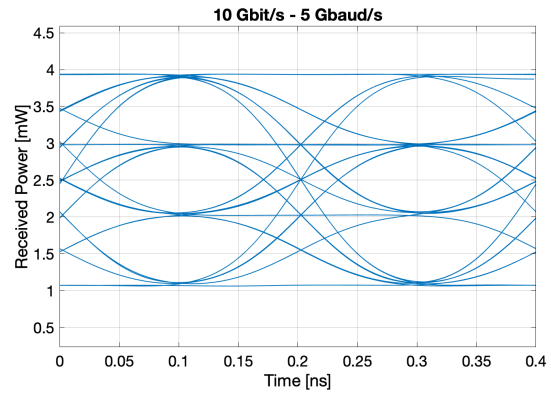


Figure 3.9: PAM-4 - Modulation current and resulting output power

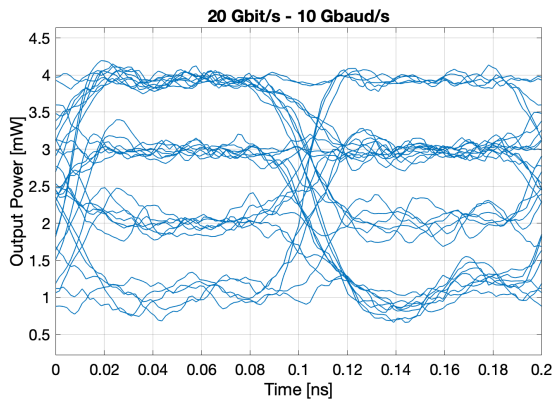
Again, the eye diagrams are reported. 40 Gbps non deve sorprendere, siamo in realta a 20 GHz, quindi nella banda di modulazione del dispositivo.



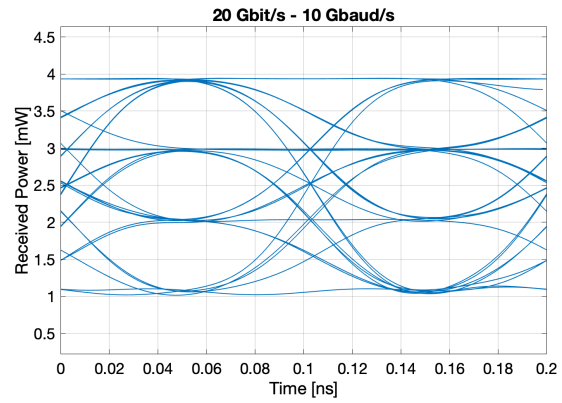
(a) 10 Gbps - Output Power



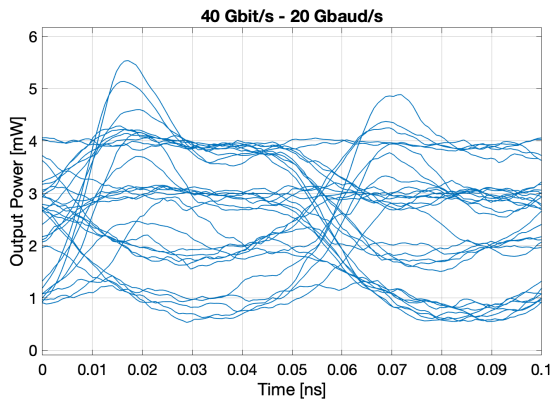
(b) 10 Gbps - Received Power



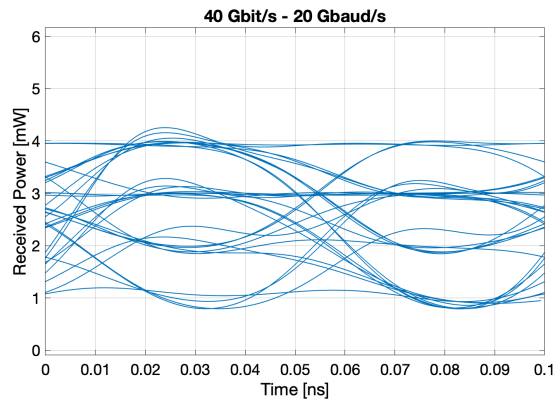
(c) 20 Gbps - Output Power



(d) 20 Gbps - Received Power



(e) 40 Gbps - Output Power



(f) 40 Gbps - Received Power

Figure 3.10: VCSEL output power - PAM-4 modulation

3.3 Conclusions

Chapter 4

Experimental measurements

After the creation and verification of the simulator results by mean of analytical formulas and provided data, the consequent step was the direct measurement of device characteristics; for this purpose OptiGOT, a startup developing VCSELs based in Gothenburg, Sweden, provided some on-wafer VCSEL samples, shown in Figure 4.1. Unfortunately, due to bureaucratic complications, the probes needed for on-chip measurements did not arrive in time.

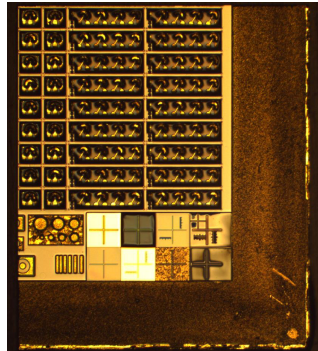
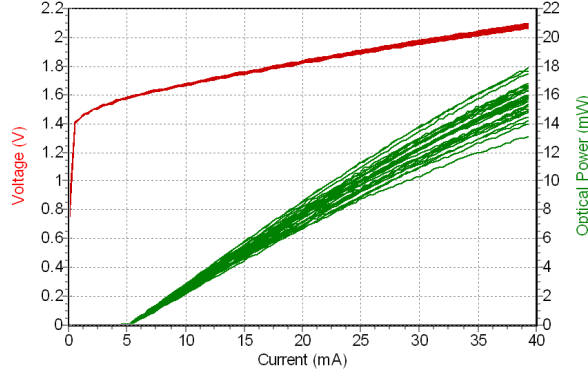


Figure 4.1: OptiGOT VCSEL samples - the overall size is around 5x4 mm

However, four VCSEL samples produced by ULM Photonics were provided by Dr. Pierluigi Debernardi. These devices were analyzed at the Photonext laboratory, in order to get confidence with the measurement instruments, and their provided characteristics are reported in Figure 4.2.

Input series resistance	14 Ω
3dB modulation bandwidth	min. 3 GHz
Threshold current	5.5 mA
RIN	-130 dB/Hz

(a) Main features



(b) PI and VI curves

Figure 4.2: ULM VCSEL - provided characteristics

The devices (one of which is shown in Figure 4.3b) were embedded in a standard LC-TOSA package, thus making the process of driving them and taking measurements easier. For this kind of packaging, in practice, the VCSEL is first embedded in a TO-46 package (Figure 4.3a), a metal case that allows the interfacing with the VCSEL through three pins (anode, cathode and case ground). Next, the metal assembly is inserted in a plastic package (LC-TOSA), that provides an extra layer of protection to the device and can include a small lens in the top aperture

In all the experiments done, as alignment of VCSEL and fiber could not be done by hand, so a Thorlabs MAX311D Fiber Alignment Stage was used (shown in Figure 4.4). Using three knobs, it allows micrometric and submicrometric movements in the x,y and z directions, allowing a precise alignment between fiber and laser. For the sake of completeness, these measurements are reported in the following. Table 4.1 reports the all the instruments used for the various measurements.

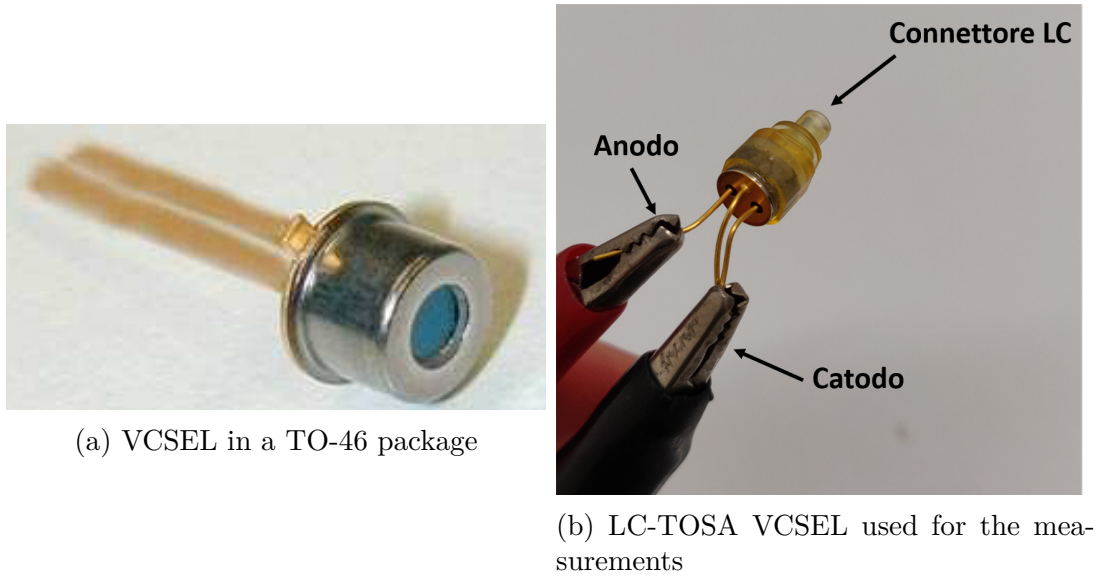


Figure 4.3: VCSEL packages



Figure 4.4: Thorlabs MAX311D Fiber alignment stage

4.1 DC characteristics - PI curve

4.1.1 Setup

For starting, DC characteristics were measured by setting up the test bench as schematized in Figure 4.5. VCSELs were current driven using a ILX Lightwave LDC-3700C Laser Driver: in order to interface the two, the VCSEL samples were soldered on a matrix board with two banana sockets embedded, that were later connected to the positive and negative terminals of the driver. The output power

Instrument type	Model
Laser Driver	ILX Lightwave LDC-3700C
Current/Voltage Meter	Fluke 45
Power Meter + Optical Head Interface	Agilent 8163B + Agilent 81619A
Fiber alignment stage	Thorlabs MAX311D
Photodiode	Newfocus 1484-A-50
Optical Spectrum Analyzer	Agilent 86140A
Network Analyzer	Agilent 8703B

Table 4.1: Laboratory equipment used

was directly measured through an Agilent 8163B power meter together with an Agilent 81619A optical head, while voltage across the VCSEL was measured using a Fluke 45 multimeter.

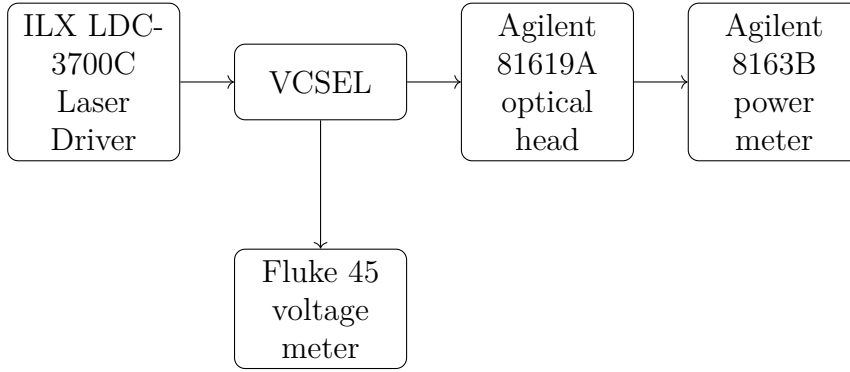


Figure 4.5: Block diagram of the DC characteristics measurement setup

4.1.2 Results

Figure 4.6 shows the PI and VI curves for the VCSELs under test. The four devices show very similar characteristics, both in terms of threshold, slope efficiency and thermal rollover. Moreover, the measurements are consistent with the provided curves, reported in Figure 4.2b.

An important aspect to take into account when measuring the characteristics of a device is the coupling loss, that is the power lost when light is coupled from the VCSEL to the fiber; one may want to keep this effect as low as possible, in order to get the most of the VCSEL output power. To evaluate this parameter, PI curve measurement were repeated by coupling a MultiMode Fiber (MMF) to the VCSEL, as schematized in the block diagram in Figure 4.7. Figure 4.8 the comparison between the two cases: fiber output power (blue curve) is much lower than directly measured power (red curve), so a considering coupling loss occurs.

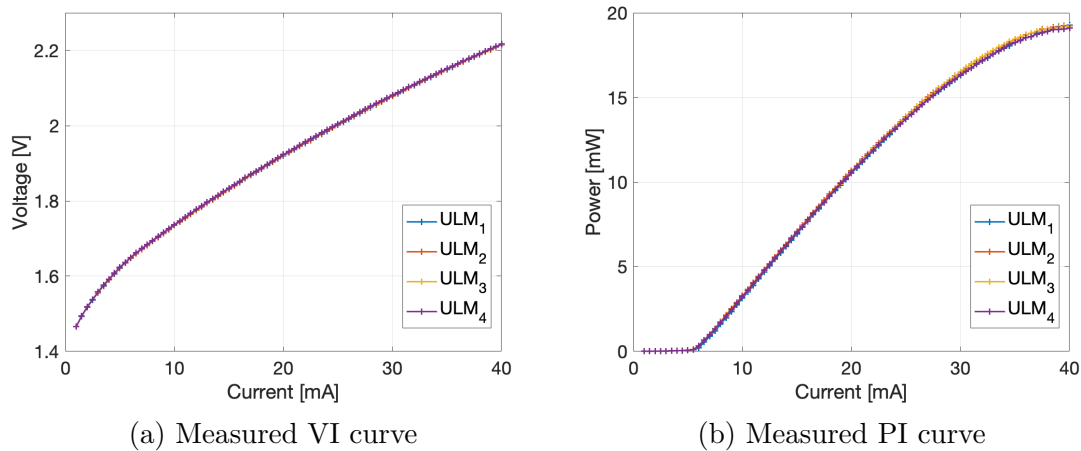


Figure 4.6: Measured DC characteristics

The large difference between the two curves can be attributed to two main effects: misalignments between the fiber and the VCSEL, since the coupling was hand-made, and permanent damages on the fiber tips, detected with a microscope check.

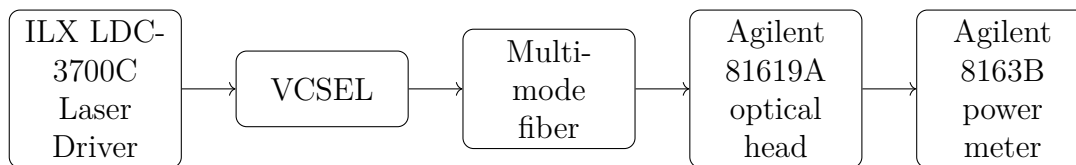


Figure 4.7: Block diagram of setup for coupling loss measurements

4.2 Electrical S-parameters

4.2.1 Setup

For the electrical S-parameters measurement, the VCSEL packages have been hand-soldered to an SMA connector. This is done for two main reasons: the first one is practical, as the Optical Spectrum Analyzer can only be interfaced via SMA ports, while the second comes from the fact that this kind of connector supports a typical passband in the 0 – 18 GHz range, making it suitable for high frequency measurements. After that, the lasers are coupled to the fiber, that is input to the Agilent 8703B Optical Spectrum Analyzer. Figure 4.9 shows the scheme of the setup just described.

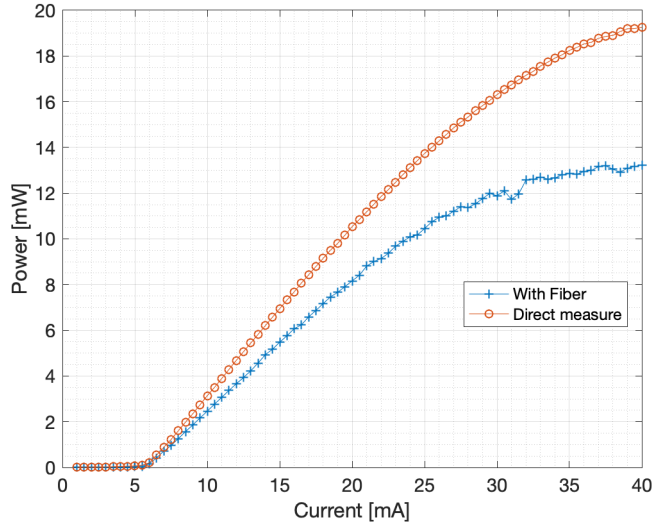


Figure 4.8: Coupling loss

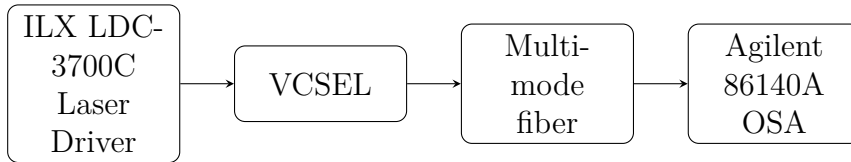


Figure 4.9: Block diagram of the S-parameters measurement setup

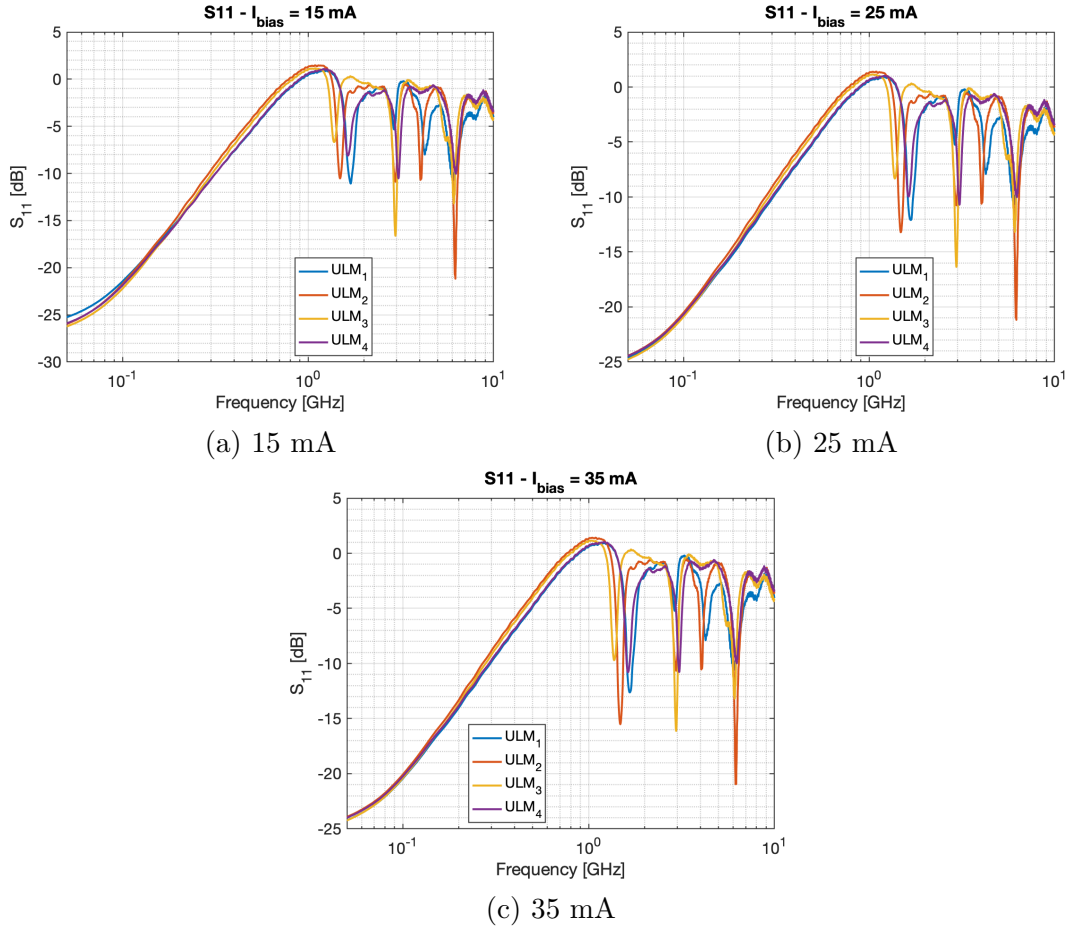
4.2.2 Results

As Figure 4.11 shows, the devices present a resonance frequency of around 3 GHz range. This is in line with the value provided by the manufacturer, as from Table 4.2a. Moreover, very relevant spurious frequency components appear at higher frequencies, probably due to parasitics deriving from the soldering process on the SMA.

4.3 Spectrum measurements

4.3.1 Setup

In order to do spectral measurements, the VCSEL was again driven by the ILX LDC-3700C Laser Driver and coupled to a multimode fiber. To interface the fiber with the Agilent 86140A Optical Spectrum Analyzer (OSA), the Newfocus 1484-A-50 photodiode was used. It has a declared bandwidth of 22 GHz, confirmed by the measurements shown in Figure 4.13. This is more than enough for measurements

Figure 4.10: Measured S_{11} response

on these devices, that, as it was shown by S-parameter measurements, have a bandwidth of around 3 GHz, as seen from the S-parameters and from the datasheet. The full chain is shown in Figure 4.12. Measurements have been obtained by driving the VCSELs with increasing current, from 7 to 30 mA.

4.3.2 Results

It is possible to see in Figure 4.14 that increasing the current leads to a shift of the VCSEL central wavelength. Furthermore, it is evident that one of the devices, shown in the figures as ULM_1 , has a central frequency that deviates of around 2 nm with respect to the others.

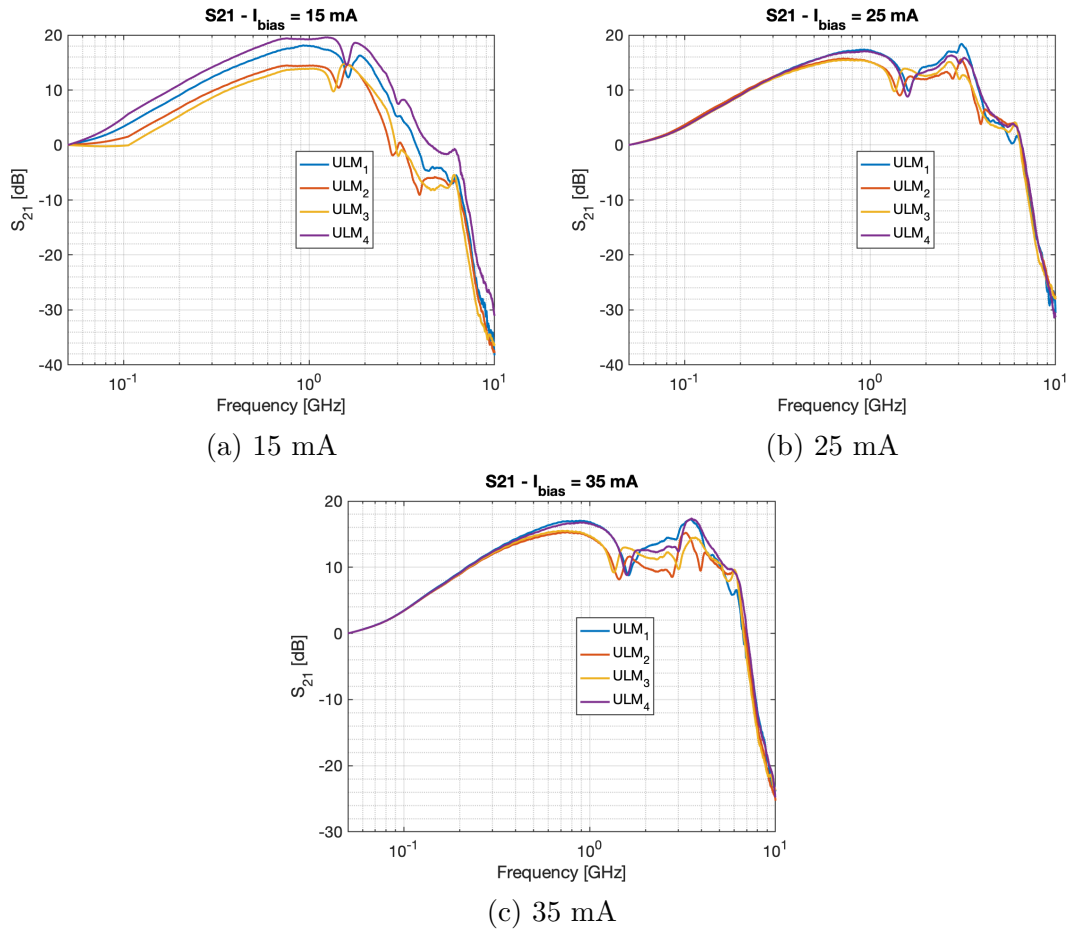


Figure 4.11: Measured S_{21} response (normalized)

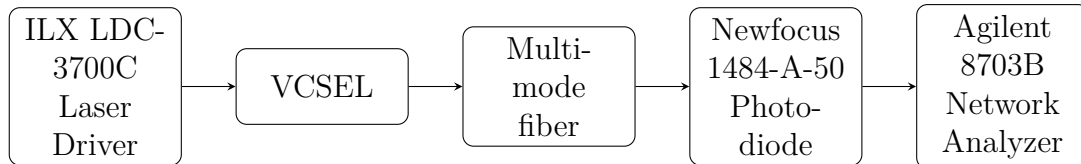


Figure 4.12: Block diagram of the spectrum measurement setup

4.4 Conclusions

By looking at the measurements, neglecting effects due to connectors or packaging inaccuracies, the measurements show almost incredible regularity when compared to the provided values. Considering that the devices were more than ten years old, this indicates the high reproducibility of VCSEL technology. On the other hand, the same effects should be considered if a batch of devices must be used. They could

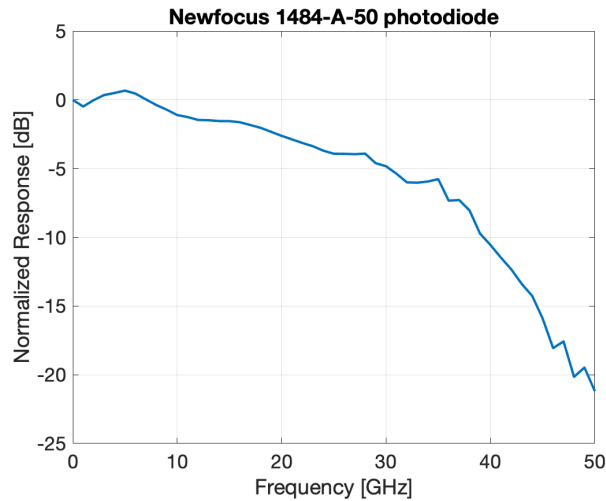


Figure 4.13: Newfocus 1484-A-50 measured frequency response

cause relevant differences in the device characteristics, so it is better to measure every device to avoid potential problems.

4.5 Appendix: hints for on-wafer measurements

Even though the on-wafer measurements were not taken, some advices are given for future reference. A reference setup for taking on-wafer device tests can be seen in Figure 4.15 (courtesy of Anders Larsson, Chalmers University). On the bottom, two brass (or copper) plates are placed, with a Peltier element in between. These help keeping constant the temperature of the device under test. An external temperature regulator (not shown) measures the temperature through the thermistor and regulates it using the Peltier cell.

On the left, the probe used for driving the device is shown; it is connected to the driving instrument through an RF cable, which transmits the input signal from the test instrument to the VCSEL. Some probe models are also shown in Figure 4.17a. On top of the device goes the fiber holder, in order to couple the output light of the device. A lens can be added between the VCSEL and the fiber, if needed. Due to the small dimensions of the bond pads used for injecting current in the VCSEL (Figure 4.16), the alignment of the probe with the wafer is not possible by hand. Typically this is done by means of a fiber alignment stage, like the one already shown in Figure 4.4. The same is valid for the fiber, as a manual alignment could cause irreversible damage both to the fiber and to the device. Figure 4.17b shows a VCSEL under test, with light directly coupled into a fiber (no lens used).

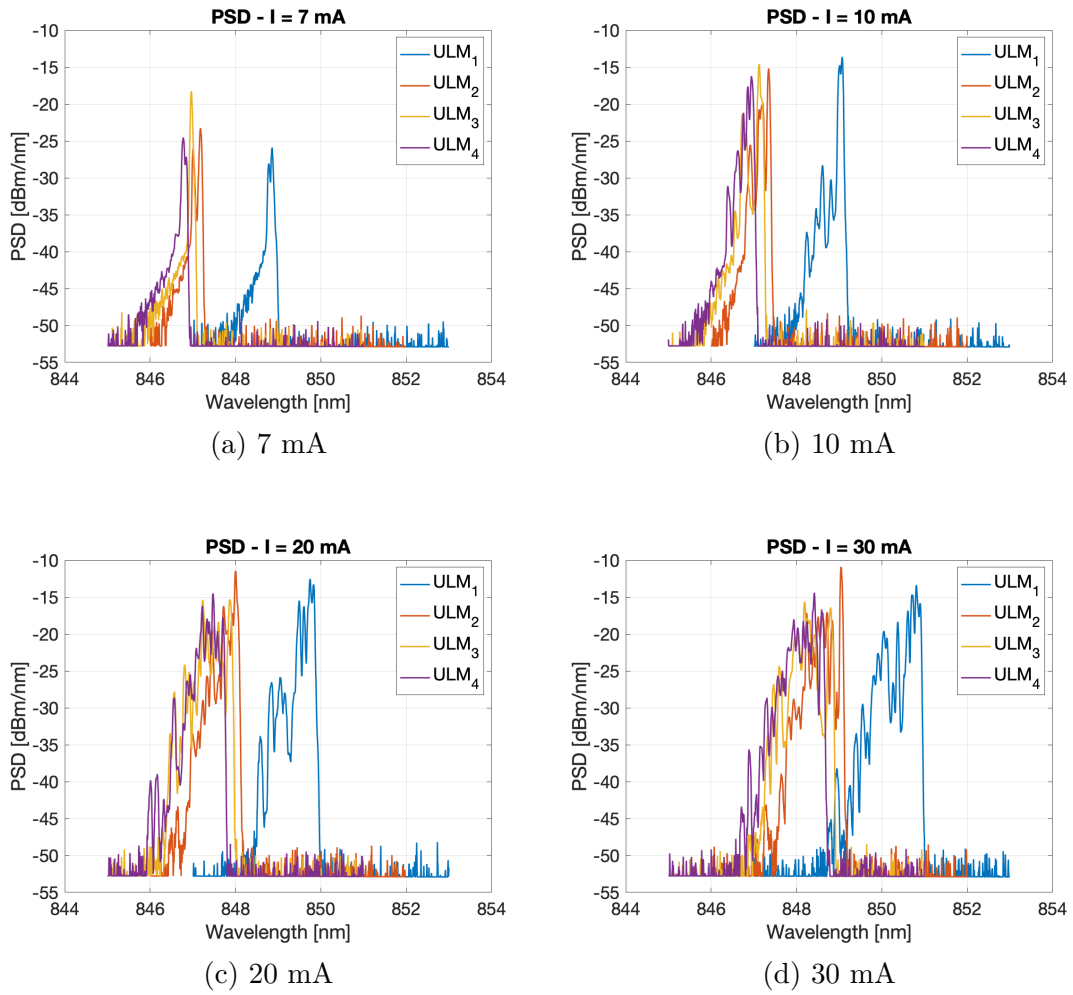


Figure 4.14: VCSEL spectra at various currents

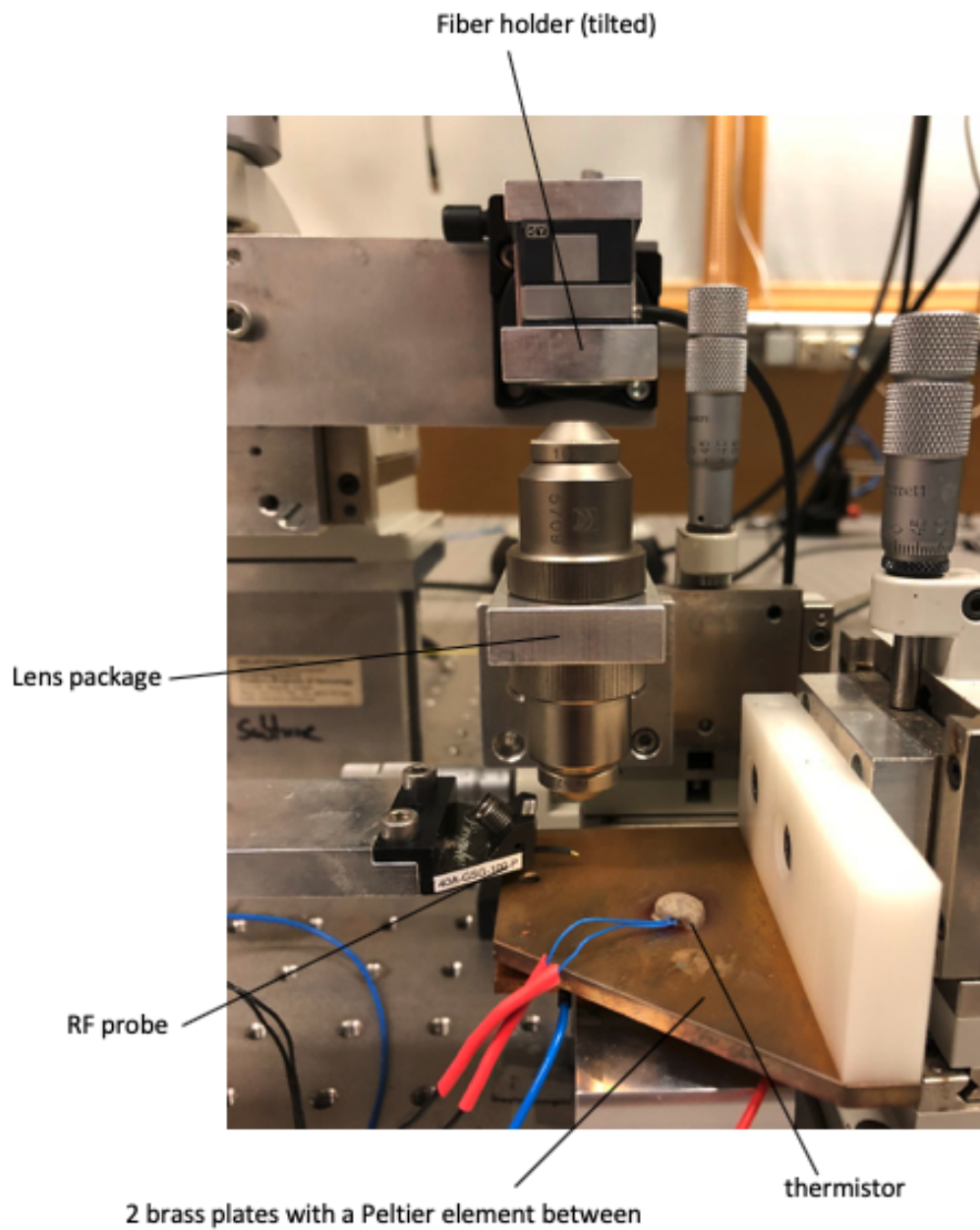


Figure 4.15: On-wafer measurement testbed

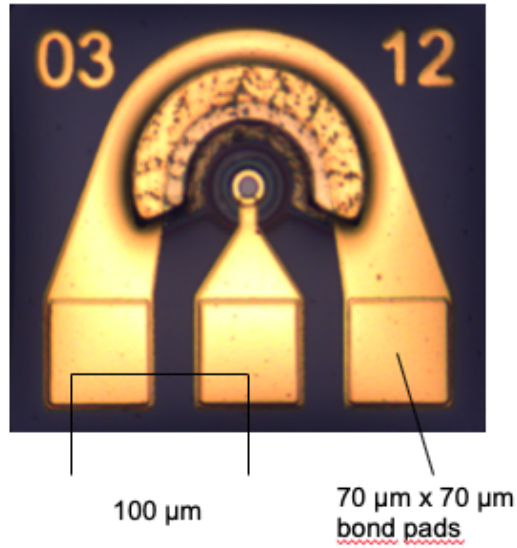
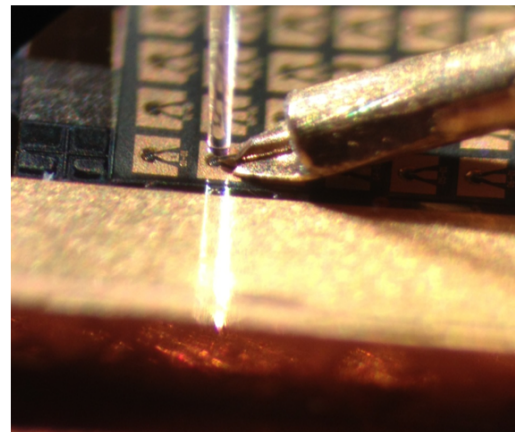


Figure 4.16: Typical dimensions of on-wafer bond pad



(a) Models of probe for on-wafer driving [48]



(b) On-wafer VCSEL measurements - the tip of the probe is visible

Figure 4.17: Probes for on-wafer testing

Chapter 5

Conclusions

Ci sono ancora strade non percorse per migliorare il simulatore: in a real life scenario, thermals are a fundamental limit when working with VCSELs, quindi si potrebbe inserire qualcosa che varia con la temperatura. Per quanto riguarda la simulazione di una trasmissione, sono stati trascurati gli effetti della fibra MMF (esistono paper?) e il rumore aggiunto dal fotodiodo a ricevitore. BER curves could be extracted after adding this parameters. Ad ogni modo, si spera che il lavoro svolto sia un buon punto di partenza per compiere simulazioni sui VCSEL.

Bibliography

- [1] Stephen Grubb et al. «Real-time 16QAM Transatlantic Record Spectral Efficiency of 6.21 b/s/Hz Enabling 26.2 Tbps Capacity». In: *Optical Fiber Communication Conference (OFC) 2019*. Optical Society of America, 2019, M2E.6. DOI: [10.1364/OFC.2019.M2E.6](https://doi.org/10.1364/OFC.2019.M2E.6). URL: <http://www.osapublishing.org/abstract.cfm?URI=OFC-2019-M2E.6>.
- [2] Cisco. *Cisco Global Cloud Index: Forecast and Methodology, 2016–2021*. URL: <https://www.cisco.com/c/en/us/solutions/collateral/service-provider/global-cloud-index-gci/white-paper-c11-738085.html> (visited on 10/28/2019).
- [3] P. C. Jain. «Recent trends in next generation terabit Ethernet and gigabit wireless local area network». In: *2016 International Conference on Signal Processing and Communication (ICSC)*. Dec. 2016, pp. 106–110. DOI: [10.1109/ICSPCom.2016.7980557](https://doi.org/10.1109/ICSPCom.2016.7980557).
- [4] The Ethernet Alliance. *2019 Roadmap*. 2019. URL: <https://ethernetalliance.org/technology/2019-roadmap/> (visited on 11/26/2019).
- [5] Haruhisa Soda et al. «GaInAsP/InP Surface Emitting Injection Lasers». In: *Japanese Journal of Applied Physics* 18.12 (Dec. 1979), pp. 2329–2330. DOI: [10.1143/jjap.18.2329](https://doi.org/10.1143/jjap.18.2329). URL: <https://doi.org/10.1143%2Fjjap.18.2329>.
- [6] K. Iga et al. «Room-temperature pulsed oscillation of GaAlAs/GaAs surface emitting injection laser». In: *Applied Physics Letters* 45.4 (1984), pp. 348–350. DOI: [10.1063/1.95265](https://doi.org/10.1063/1.95265). eprint: <https://doi.org/10.1063/1.9526>. URL: <https://doi.org/10.1063/1.95265>.
- [7] Jim A. Tatum et al. «Commercialization of Honeywell’s VCSEL technology». In: *Vertical-Cavity Surface-Emitting Lasers IV*. Ed. by Kent D. Choquette and Chun Lei. Vol. 3946. International Society for Optics and Photonics. SPIE, 2000, pp. 2–13. DOI: [10.1117/12.384359](https://doi.org/10.1117/12.384359). URL: <https://doi.org/10.1117/12.384359>.

- [8] F. Koyama and X. Gu. «Beam Steering, Beam Shaping, and Intensity Modulation Based on VCSEL Photonics». In: *IEEE Journal of Selected Topics in Quantum Electronics* 19.4 (July 2013), pp. 1701510–1701510. DOI: [10.1109/JSTQE.2013.2247980](https://doi.org/10.1109/JSTQE.2013.2247980).
- [9] Ahmed Al-Samaneh et al. «Polarization Control and Dynamic Properties of VCSELs for MEMS Atomic Clock Applications». eng. In: *IEEE Photonics Technology Letters* 23.15 (2011), pp. 1049–1051. ISSN: 1041-1135.
- [10] Ahmed Al-Samaneh et al. «Polarization-stable single-mode VCSELs for Cs-based MEMS atomic clock applications». In: *Semiconductor Lasers and Laser Dynamics IV*. Ed. by Krassimir Panajotov et al. Vol. 7720. International Society for Optics and Photonics. SPIE, 2010, pp. 38–51. DOI: [10.1117/12.853181](https://doi.org/10.1117/12.853181). URL: <https://doi.org/10.1117/12.853181>.
- [11] M. J. Miah et al. «Fabrication and Characterization of Low-Threshold Polarization-Stable VCSELs for Cs-Based Miniaturized Atomic Clocks». In: *IEEE Journal of Selected Topics in Quantum Electronics* 19.4 (July 2013), pp. 1701410–1701410. DOI: [10.1109/JSTQE.2013.2247697](https://doi.org/10.1109/JSTQE.2013.2247697).
- [12] Naotaka Mukoyama et al. «VCSEL array-based light exposure system for laser printing». In: *Vertical-Cavity Surface-Emitting Lasers XII*. Ed. by Chun Lei and James K. Guenter. Vol. 6908. International Society for Optics and Photonics. SPIE, 2008, pp. 146–156. DOI: [10.1117/12.768479](https://doi.org/10.1117/12.768479). URL: <https://doi.org/10.1117/12.768479>.
- [13] A.E. Elsner and M.S. Muller. «Laser applications and system considerations in ocular imaging». In: *Laser & Photonics Reviews* 2.5 (2008), pp. 350–376. DOI: [10.1002/lpor.200810015](https://doi.org/10.1002/lpor.200810015). eprint: <https://onlinelibrary.wiley.com/doi/pdf/10.1002/lpor.200810015>. URL: <https://onlinelibrary.wiley.com/doi/abs/10.1002/lpor.200810015>.
- [14] T. P. Butler et al. «Real-Time Experimental Measurement of Swept Source VCSEL Properties Relevant to OCT Imaging». In: *IEEE Photonics Journal* 9.5 (Oct. 2017), pp. 1–10. DOI: [10.1109/JPHOT.2017.2752644](https://doi.org/10.1109/JPHOT.2017.2752644).
- [15] E. Thiel, M. Ziegler, and T. Studemund. «Localization of Subsurface Defects in Uncoated Aluminum with Structured Heating Using High-Power VCSEL Laser Arrays». In: *International Journal of Thermophysics* 40.2 (Jan. 2019), p. 17. ISSN: 1572-9567. DOI: [10.1007/s10765-018-2478-9](https://doi.org/10.1007/s10765-018-2478-9). URL: <https://doi.org/10.1007/s10765-018-2478-9>.
- [16] Pierrick Boulay. «After 20 years, the VCSEL business has found its killer application - and is likely to explode». In: (VCSEL Day 2019, Apr. 12, 2019).
- [17] L. A. Coldren, S. W. Corzine, and Milan Masanovitch. *Diode lasers and photonic integrated circuits*. Wiley, 2012.

- [18] Michael T. Lapp. «Deposition and Characterization of Dielectric Distributed Bragg Reflectors». In: 2016.
- [19] Emanuel Haglund. *Vertical-Cavity Surface-Emitting Lasers: Large Signal Dynamics and Silicon Photonics Integration*. eng. 2016.
- [20] Pierluigi Debernardi. *Vertical Cavity Surface Emitting Lasers (VCSELs): Basics and Applications*. Apr. 2018.
- [21] K. Takaki. «A recorded 62% PCE and low series and thermal resistance VCSEL with a double intra-cavity structure». In: *21st ISLC, Sept. 2008* (2008), pp. 1–2. URL: <https://ci.nii.ac.jp/naid/20000754061/en/>.
- [22] Infiniband Trade Association. *Infiniband Roadmap*. 2019. URL: <https://www.infinibandta.org/infiniband-roadmap/> (visited on 11/26/2019).
- [23] Fibre Channel Industry Association. *Fibre Channel Roadmap*. 2019. URL: <https://fibrenchannel.org/roadmap/> (visited on 11/30/2019).
- [24] K. Iga. «Surface-emitting laser-its birth and generation of new optoelectronics field». In: *IEEE Journal of Selected Topics in Quantum Electronics* 6.6 (Nov. 2000), pp. 1201–1215. ISSN: 1558-4542. DOI: [10.1109/2944.902168](https://doi.org/10.1109/2944.902168).
- [25] Zhongwei Tan et al. «A 70 Gbps NRZ optical link based on 850 nm band-limited VCSEL for data-center intra-connects». In: *Science China Information Sciences* 61.8 (Feb. 2018), p. 080406. ISSN: 1869-1919. DOI: [10.1007/s11432-017-9276-y](https://doi.org/10.1007/s11432-017-9276-y). URL: <https://doi.org/10.1007/s11432-017-9276-y>.
- [26] Krzysztof Szczerba et al. «60 Gbits error-free 4-PAM operation with 850 nm VCSEL». eng. In: *Electronics Letters* 49.15 (2013), pp. 953–955. ISSN: 0013-5194.
- [27] F. Karinou et al. «112 Gb/s PAM-4 Optical Signal Transmission over 100-m OM4 Multimode Fiber for High-Capacity Data-Center Interconnects». In: *ECOC 2016; 42nd European Conference on Optical Communication*. Sept. 2016, pp. 1–3.
- [28] Hamed Dalir and Fumio Koyama. «29 GHz directly modulated 980 nm vertical-cavity surface emitting lasers with bow-tie shape transverse coupled cavity». In: *Applied Physics Letters* 103.9 (2013), p. 091109. DOI: [10.1063/1.4820149](https://doi.org/10.1063/1.4820149). eprint: <https://doi.org/10.1063/1.4820149>. URL: <https://doi.org/10.1063/1.4820149>.
- [29] E. Simpanen et al. «1060 nm Single-Mode VCSEL and Single-Mode Fiber Links for Long-Reach Optical Interconnects». In: *Journal of Lightwave Technology* 37.13 (July 2019), pp. 2963–2969. DOI: [10.1109/JLT.2019.2908249](https://doi.org/10.1109/JLT.2019.2908249).
- [30] C. Kocot et al. «SWDM strategies to extend performance of VCSELs over MMF». In: *2016 Optical Fiber Communications Conference and Exhibition (OFC)*. Mar. 2016, pp. 1–3.

-
- [31] Christian Urricariet. *SWDM: The Lowest Total Cost Solution for 40G/100G in the Enterprise Data Center*.
- [32] J. Lavrencik et al. «Scaling VCSEL-MMF Links to 1 Tb/s Using Short Wavelength Division Multiplexing». In: *Journal of Lightwave Technology* 36.18 (Sept. 2018), pp. 4138–4145. ISSN: 1558-2213. DOI: [10.1109/JLT.2018.2858208](https://doi.org/10.1109/JLT.2018.2858208).
- [33] Christian Urricariet. *SWDM: The Lowest Total Cost Solution for 40G/100G in the Enterprise Data Center*. Oct. 2018.
- [34] Arman Shehabi et al. *United States Data Center Energy Usage Report*. June 2016.
- [35] Erik Haglund. *VCSELs for High-Speed, Long-Reach, and Wavelength-Multiplexed Optical Interconnects*. eng. 2015.
- [36] J. B. Héroux et al. «Energy-Efficient 1060-nm Optical Link Operating up to 28 Gb/s». In: *Journal of Lightwave Technology* 33.4 (Feb. 2015), pp. 733–740. ISSN: 1558-2213. DOI: [10.1109/JLT.2015.2393888](https://doi.org/10.1109/JLT.2015.2393888).
- [37] E. Haglund et al. «30 GHz bandwidth 850 nm VCSEL with sub-100 fJ/bit energy dissipation at 25–50 Gbit/s». In: *Electronics Letters* 51.14 (2015), pp. 1096–1098. DOI: [10.1049/el.2015.0785](https://doi.org/10.1049/el.2015.0785).
- [38] R. Michalzik. *VCSELs: Fundamentals, Technology and Applications of Vertical-Cavity Surface-Emitting Lasers*. Springer Series in Optical Sciences. Springer Berlin Heidelberg, 2012. ISBN: 9783642249860. URL: <https://books.google.it/books?id=1-y5BQAAQBAJ>.
- [39] M. Streiff et al. «A comprehensive VCSEL device simulator». In: *IEEE Journal of Selected Topics in Quantum Electronics* 9.3 (May 2003), pp. 879–891. ISSN: 1558-4542. DOI: [10.1109/JSTQE.2003.818858](https://doi.org/10.1109/JSTQE.2003.818858).
- [40] Alberto Tibaldi et al. «VENUS: A Vertical-Cavity Surface-Emitting Laser Electro-Opto-Thermal NUMerical Simulator». eng. In: *IEEE Journal of Selected Topics in Quantum Electronics* 25.6 (2019), pp. 1–12. ISSN: 1077-260X.
- [41] Inc. Synopsis. *LaserMOD Product Overview*. 2019. URL: <https://www.synopsys.com/optical-solutions/rsoft/active-device-lasermod.html> (visited on 11/26/2019).
- [42] Crosslight Software. *PICS3D*. 2019. URL: <https://crosslight.com/products/pics3d/> (visited on 11/28/2019).
- [43] Yang Liu et al. «Effects of the spatial nonuniformity of optical transverse modes on the modulation response of vertical-cavity surface-emitting lasers». In: *IEEE Journal of Quantum Electronics* 39.1 (Jan. 2003), pp. 99–108. ISSN: 1558-1713. DOI: [10.1109/JQE.2002.806205](https://doi.org/10.1109/JQE.2002.806205).

- [44] B. Zhao, T. R. Chen, and A. Yariv. «The gain and carrier density in semiconductor lasers under steady-state and transient conditions». In: *IEEE Journal of Quantum Electronics* 28.6 (June 1992), pp. 1479–1486. ISSN: 1558-1713. DOI: [10.1109/3.135300](https://doi.org/10.1109/3.135300).
- [45] Pierluigi Debernardi et al. «Probing Thermal Effects in VCSELs by Experiment-Driven Multiphysics Modeling». eng. In: *IEEE Journal of Selected Topics in Quantum Electronics* 25.6 (2019), pp. 1–14. ISSN: 1077-260X.
- [46] B. Weigl et al. «High-performance oxide-confined GaAs VCSELs». In: *IEEE Journal of Selected Topics in Quantum Electronics* 3.2 (Apr. 1997), pp. 409–415. ISSN: 1558-4542. DOI: [10.1109/2944.605686](https://doi.org/10.1109/2944.605686).
- [47] Le Nguyen Bihn. *Optical fiber communications systems : theory and practice with MATLAB and Simulink models / Le Nguyen Binh*. eng. Boca Raton: CRC Press, 2010. ISBN: 9781439806203.
- [48] GGB Industries Inc. *Model 50A High Performance Microwave Probes*. URL: http://www.ggb.com/PdfIndex_files/mod50a.pdf (visited on 10/28/2019).